Evolution of normal faults and fault-related damage: insights from physical experiments

Ingvild Blækkan

Thesis for the degree

Master of Science

Department of Earth Science

UNIVERSITY OF BERGEN

June 2016

Abstract

Our understanding of the growth of natural extensional faults is limited to the study of a random snapshot in time, namely that of present day, aided by various techniques to reconstruct fault growth history. Furthermore, whilst the growth of faults may to some extent be reconstructed, the evolution of fault-related damage is harder to reconstruct and less well understood. In this study we use physical analogue plaster models to study fault evolution in extensional regimes in time and space. The resulting fault systems have been analysed based on photos, videos, and the final preserved model itself.

Fault growth analyses from the plaster models show that not all faults follow the same pathway for growth. Some faults link up with adjacent faults and grow via sympathetic increase of displacement and length, whereas others show a more rapid establishment of the final fault length, with only minor fault tip propagation as additional displacement is accumulated. Other faults use some time to establish their final fault length, and once the length is established, displacement is accumulated.

A characterisation of the topology of fault and fracture networks in analogue single-phase models is quantified. The results show that the proportion of splaying and abutting nodes (Y-nodes) increases at the expense of isolated nodes (I-nodes) as the strain increases. These changes are especially noticeable in the hanging wall to the main fault in the studied system. Also the proportion of fully connected branches (C-C branches) and partly connected branches (I-C branches) increases with increasing strain whereas the proportion of isolated branches (I-I branches) decreases. This emphasises that the connectivity in a fault and fracture network increases with increasing strain. Contour plots of connecting node frequency and branch intensity from the analysed models gain insight into the spatial distribution of areas with higher connectivity. These plots reveal that areas with high connecting node frequency coincide with areas with high branch intensity, suggesting that the connectivity increases with increasing deformation.

Based on the analysis of analogue plaster models, it becomes clear that such forward modelling provides valuable insight into fault and damage-zone evolution that can be used to get a better understanding of fault growth, damage evolution and connectivity.

Acknowledgement

I would like to take this opportunity to thank all the people that have contributed during the work with my master thesis. First of all I would like to thank my main supervisor Atle Rotevatn (University of Bergen, Department of Earth Science) for his valuable inputs and support during the last two years. I would also like to thank my co-supervisors Haakon Fossen (University of Bergen, Department of Earth Science) for helpful comments on the written work and Eivind Bastesen (Centre for Integrated Petroleum Research, University of Bergen) for inputs in the experimental work. Also a great thanks to Casey Nixon (University of Bergen, Department of Earth Science) for taking his time to teach me ArcGIS and valuable inputs in the written part. I would also like to thank Josef Kurtis for excellent carpentry with the deformation rig.

Thanks to Statoil and University of Bergen for funding this project.

Secondly, I would like to thank my friends Maria Seim and Margrethe Bøyum for all the help I got during the experimental work. I would also like to use this opportunity to thank all of the students that assisted with cameras and lighting during the experiments.

In the end, I would like to use this opportunity to thank all my friends and family for encouragement and motivation throughout the last five years, especially Vilde, Maria, Birgitte and the rest of the people at Hjørnerommet. Special thanks to Felix for the all the support and for taking the time to proof-read parts of my master thesis.

Bergen 01.06.2016

Ingvild Blækkan

Contents

CHAPTER 1 - INTRODUCTION

1.1 Background and rationale

It is important to understand the evolution and characteristics of faults and their damage zones. Firstly, the evolution of faults and damage zones are fundamental processes which applies to basin formation, fluid flow in the subsurface and fluid rock interaction. Secondly, knowledge about normal fault geometry and evolution can be valuable in the petroleum industry as faults provide important migration pathways from source to reservoir rock. Large scale faults and geological structures can be imaged and interpreted in both 2D and 3D seismic data. However, seismic data do not provide information about small-scale faults with throw less than 15-20 metre due to the resolution (Fossen, 2010, p.162). Structures like relay ramps, lenses and drag zones may therefore not be visible in the datasets. By studying analogue models, scientists get a better understanding of how faults evolve with time and space and the opportunity to look at the 3D geometry of the faults. Observations from the field only show the current snap shot, and usually exposure of the outcrop is limited, allowing only 2D studies.

Work with topology of fracture network have been done to evaluate the connectivity of fault and fracture networks (e.g. Manzocchi (2002), Sanderson and Nixon (2015), Morley and Nixon (2016)). The topology is a quantitative measurement to assess the connectivity of a fault and fracture network which is important to understand in terms of fluid flow. A topological analysis of the damage zone in the hanging wall and footwall do not only consider their geometric properties such as length, spatial orientation and intensity, but also the relationship between different faults and fractures. By characterising the topology of fault and fracture systems, the relationship between single faults and fractures can be better described.

To get a better understanding of fault growth and evolution of damage zones, analogue plaster models have been carried out in the lab. Analogue physical modelling is a well-known method attempting to simulate the deformation of the brittle upper crust. Such forward modelling can provide information on how complex geological structures evolve with time and space, and give geologists the opportunity to observe how new faults form, and how single faults link up together to a final complex fault system (McClay, 1996). The most commonly used materials are sand, clay and plaster, either alone or in combination with less

common materials such as barite or putty honey. Previous analogue models have shown that the structures found in the nature are similar to the ones made in the lab, e.g. Gullfaks field (Fossen and Gabrielsen, 1996) and Outer Moray Firth (Higgs and McClay, 1993). This emphasises that the models made for this thesis can be used as a tool to improve the understanding of the evolution of faults and their damage zones.

1.2 Aims and objectives

The main aim of this master thesis is to create realistic analogue models of extensional regimes to gain insight into fault growth, damage zone evolution and to get a better understanding of how the topology and thus connectivity of a fault system evolves with increasing strain. The analysis of the model will focus on:

- How do faults grow and link to form longer amalgamated faults?
- How does fault-related damage evolve over time?
- How does the topology, and thus connectivity, of the studied fault system evolve over time in the hanging wall and footwall?

The results from the analogue plaster models are later interpreted and placed in a bigger picture where they are compared with similar structures found in nature.

CHAPTER 2 – EXTENSIONAL FAULTS AND FAULT-RELATED STRUCTURES

2.1 Introduction

The aim of this chapter is to provide necessary information about fault architecture, fault growth and linkage, with a focus on structures found in an extensional setting and analogue models presented in the result chapter. An explanation of topology will be presented at the end of this chapter.

Extensional normal faults are commonly found in rift system where continental lithosphere undergoes regional horizontal stretching. The lithosphere is stretched more or less perpendicular to the fault array. There are several reasons for rifting to occur, although some of them are more common and severe than others. One reason for extension is tectonic stress related to plate tectonics or rising of hot magma from the asthenosphere, causing tension stress to the lithosphere (Fossen, 2010, p.342-342). This results in stretching of the crust and normal faults developing in the upper part of the lithosphere. Another reason for rifting is the gravitational force. This occurs in regions with thick continental crust like an orogenesis. The lower crust is softened at great depth, and gravitational potential energy causes the thickened zone to collapse under its own weight, called extensional collapse (Van der Pluijm and Marshak, 2004, p.408-410).

2.2 Fault architecture

A fault zone commonly includes a fault core and a damage zone surrounding the fault core (Fig. 2.1). It is no scalar relationship between the different components and not all of them have to be present at any time (Caine et al., 1996).

The fault core is defined as the zone where most of the displacement is accommodated (Caine et al., 1996), and can include a single slip surface, altered rock, fault rocks, lenses, shale smear and fractures (Caine et al., 1996, Braathen et al., 2009). The thickness of the fault core varies along both the strike and slip direction. During deformation, the fault zone may act as a migration pathway for fluids. With time, precipitation of secondary minerals may fill the pore space along the fault zone, and the fault zone will then become a barrier for fluid migration (Caine et al., 1996).

The damage zone defines the zone around the fault core with a higher density of deformation than the protolith (Cowie and Scholz, 1992a, Kim et al., 2004). Damage zone structures include deformation bands, tensile fractures and shear fractures (Braathen et al., 2009). Kim et al. (2004) has characterised and divided the damage zone into zones; tip-damage zone, wall damage zone and linkage damage zone.

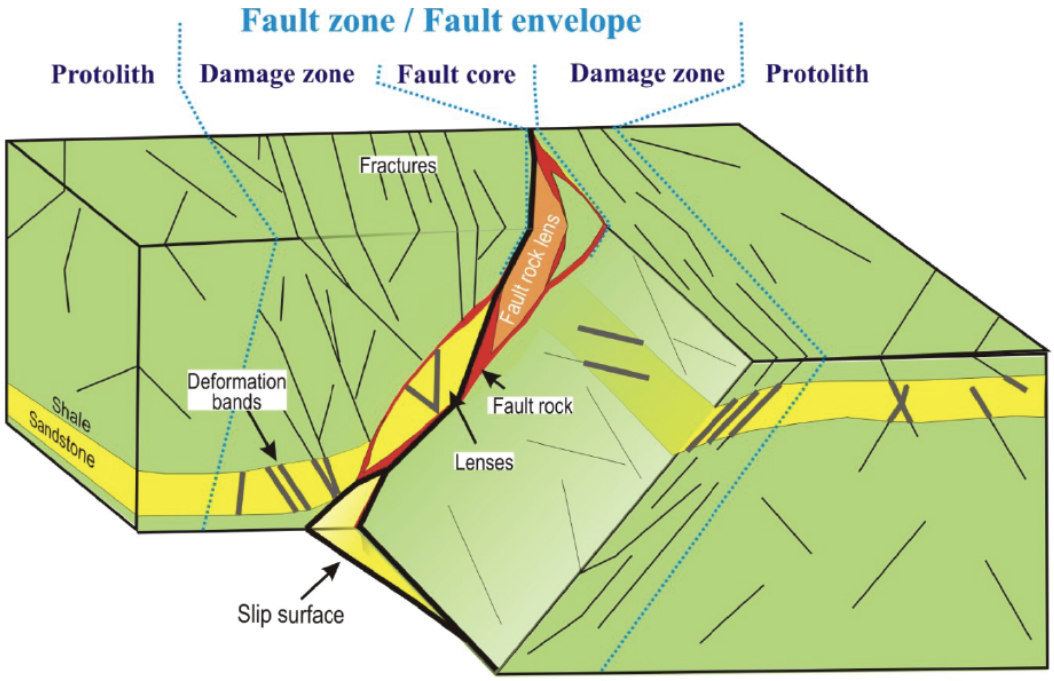

Fig. 2.1: Illustration of the fault core and the surrounding damage zone, including common structures found in relationship to fault zones. Modified from Braathen et al. (2009).

2.3 Fault growth

2.3.1 Fault growth by a single fault

It is important to understand the spatial evolution of single faults. Field observations have shown that there is a positive correlation between fault length (L) and displacement (D) along the fault (Cowie and Scholz, 1992a). The displacement of the fault is zero at the fault tip, and increases toward the centre of the fault, with a maximum displacement in the centre (Kim and Sanderson, 2005). This means that the fault plane has to be elliptical. A relationship between the maximum displacement (D) and the fault length (L) have been developed. $D=cL^n$, where c is dependent on the properties of the material and the value of n varies from 0.5 to 2.0 in different datasets (e.g. n = 0.5, Fossen and Hesthammer (1997); n = 1.0, Cowie and Scholz (1992c), Schlische et al. (1996); n = 1.5, Gillespie et al. (1992); n = 2.0, Walsh and Watterson

(1988)). The value of n indicates if there is a linear relation or not between length and displacement, if $n = 1$ there is a linear relationship.

This relationship can only be used at bounded faults because the displacement increases as the strain is accumulated. Unbounded faults, such as San Andreas fault zone are controlled by plate tectonics and geometry, and the relation between displacement and fault length is therefore not representative (Cowie and Scholz, 1992a).

2.3.2 Normal fault growth models

Two models for normal fault growth have been postulated. One model is characterized by isolated faults growing by radical propagation and eventually linkage (e.g. Cowie and Scholz (1992b), Cartwright et al. (1995), Rykkelid and Fossen (2002)). This model is known as the "isolated fault model" (Walsh et al., 2003) or "fault growth by segment linkage" (Cartwright et al., 1995). The second model for fault growth is known as the "alternative growth model" (Walsh et al., 2002) or "coherent fault model" (Walsh et al., 2003) (Fig. 2.2) where fault segments appear as isolated faults at the surface, and are kinematically related in the subsurface (Walsh et al., 2002, Walsh et al., 2003). The fundamental differences between the two models is that in the "isolated fault model" each fault is initially isolated and unrelated to the fault array, whereas in the "coherent fault model" faults appear as isolated at the surface, but are kinematically coupled, or "coherent", from their inception.

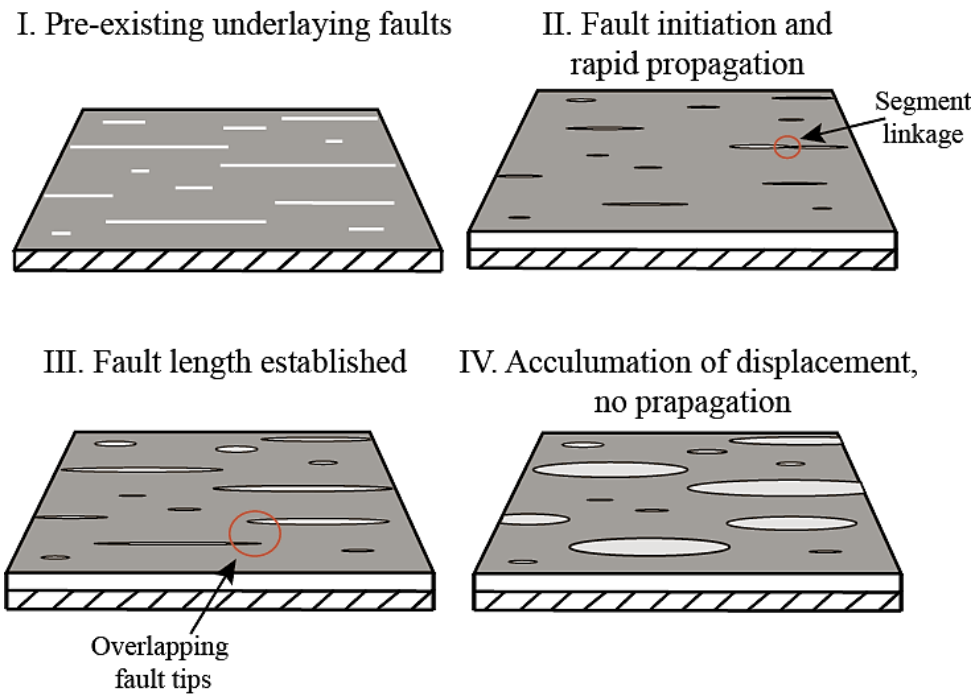

Fig. 2.2: Fault growth model suggested by Walsh et al. (2002). The faults show a rapid propagation to a final fault length, and then displacement accumulation. Redrawn after Walsh et al. (2002).

A relay ramp (Fig. 2.3a) is defined as a transfer zone that occurs between normal fault segments having the same dip direction (Larsen, 1988). Relay ramps are common in extensional basins, link the hanging wall and footwall together, and can therefore be an important migration pathway for hydrocarbons. Hydrocarbons can also be trapped in the relay ramp due to folding and faulting (Peacock and Sanderson, 1994). Folding of the relay ramp results in development of veins and faults across the ramp which eventually may connect the two segments. Relay ramps also create subsidence and half grabens. Associated structures are hanging wall down wrap, footwall uplift and rollover down wrap. These structures control local drainage, erosion, sedimentation and facies distribution (Larsen, 1988). With increasing strain, the two faults connected by the relay ramp will eventually link together. The linking of the two faults can develop in several ways. "Mid-ramp" breach (Fig. 2.3b) is characterized by fault splay at both linked faults. "Single tip" breached relay ramps (Fig. 2.3c) are where the relay itself is preserved, either in the hanging wall (lower breached) or footwall (upper breached). In a "double" breached relay ramp (Fig. 2.3d) both fault tips curve toward the opposite fault, resulting in preservation of the relay ramp as a "lens" at the slip surface (Fossen and Rotevatn, 2016).

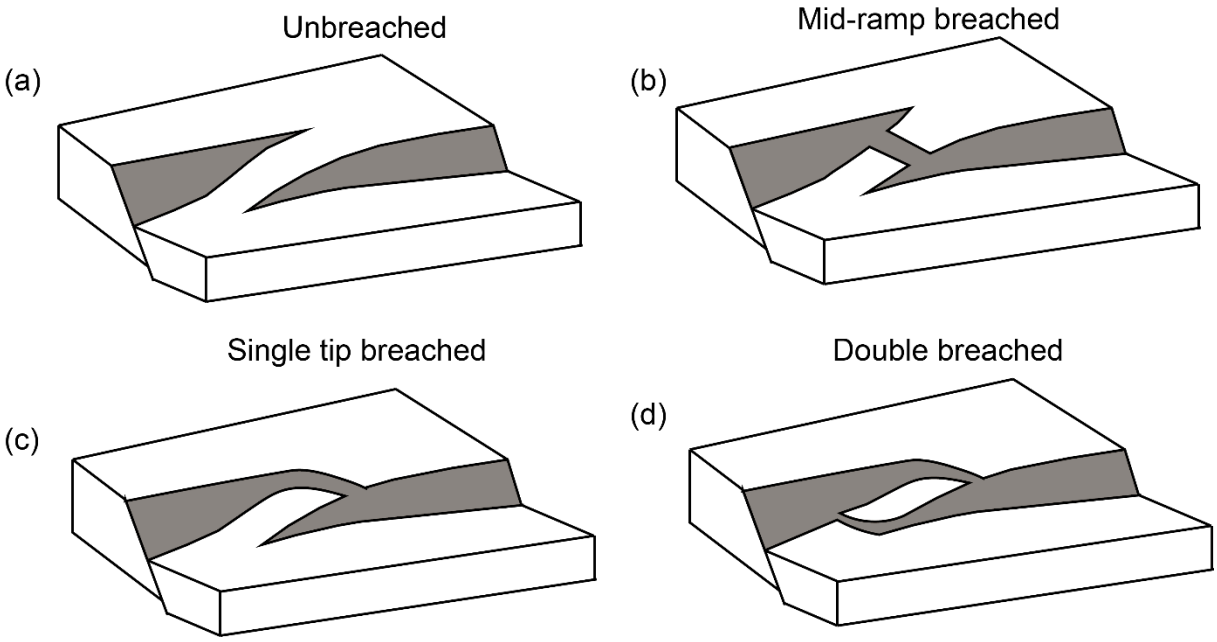

Fig. 2.3: Illustrations of breached relay ramps. The grey areas represent the slip surfaces of the faults. (a) Unbreached relay ramp, (b) mid-ramp breached relay ramp, (c) single tip breached relay ramp and (d) double breached relay ramp.

The growth by linkage of fault segments can be divided into four different stages, including breaching of the ramp. This development and evolution of relay ramps is well described by Peacock and Sanderson (1994).

1. *Isolated faults:* The fault segments are isolated and do not interact with each other. The maximum displacement is close to the centre of each fault and decreases toward the fault tips where it is zero.
2. *Interaction and ramp development:* The faults propagate toward one another and interact, but do not connect. The two overlapping fault segments create a relay ramp, connecting the hanging wall with the footwall. The bedding in the ramp usually has a rotation toward the hanging wall (Peacock and Sanderson, 1994).
3. *Fracture development across the relay ramp:* This stage is characterised by faults and fractures cutting the relay ramp. Bending and twisting of the relay ramp result in rotation of beds within the ramp. The beds are typically rotated toward the hanging wall.
4. *Breaching of the ramp:* Segments are connected, hard linked, and the relay ramp is breached. The linkage of fault segments is preserved as normal drag and causes a decrease in displacement at the connection point (Peacock and Sanderson, 1991), and two maxima on each side of the linked area. Linked fault segments typically result in a curved geometry along the fault zone in the linkage area.

2.5 Topology

The major controls on the arrangement of fractures within a fault network are poorly understood. It is important to understand the topology of a fracture network. Two fault systems can contain the same geometrical elements, but have different topology. Topology is an important factor in describing the relationship between geometrical elements found in fault zones and fault systems.

The topology of a fault and fracture network can be considered in terms of nodes and branches (Fig. 2.4). Nodes can be divided into three classes. I-nodes represent the isolated fault tips of faults and fractures, Y- and X-nodes represent the intersecting point of two fractures, as either splaying or abutting (Y-nodes) or crossing (X-nodes). Branches are defined from the different nodes at each end, and are classified as isolated branch (I-I), partly connected branch (I-C) or fully connected branch (C-C) (Manzocchi, 2002, Sanderson and Nixon, 2015). The number and the ratio between nodes and branches in a fault and fracture

system define the network topology and these values can be plotted in triangular diagrams to quantify the connectivity in a fault and fracture network.

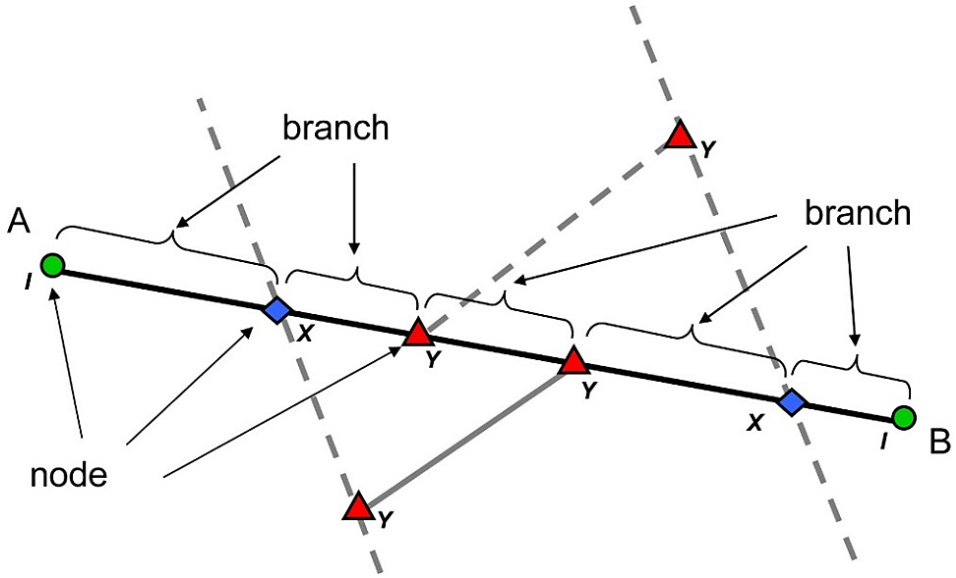

Fig. 2.4: Fracture from A to B with additional nodes and branches. Dashed lines represent intersecting fractures. I-nodes shown as circles, Y-nodes as triangles and X-nodes as diamonds. From Sanderson and Nixon (2015).

Topology is an important tool for assessing the connectivity in a fracture network. A network which only consists of I-I branches will not have any connections. A network dominated by I-I breaches will therefore have a very low connectivity. If the network is dominated by I-C branches, small clusters with connected branches will develop. This is characterising for splaying faults. In an I-C branch dominated network, the connection and the ability for a fluid to percolate between the different clusters are small, and the connectivity is therefore still quite low. In networks dominated by C-C branches, the clusters of connecting branches are larger and better connected, and the ability for fluids to percolate is better, ergo, the connectivity is better.

CHAPTER 3 – THEORETICAL BACKGROUND OF ANALOGUE MODELLING

3.1 Introduction

Analogue modelling of faulting has been used to emulate a wide range of deformation structures in natural rocks over the last century. Analogue models of extensional, contractional and strike-slip regimes have given geologists insight into the evolution of faults and the processes related to faulting such as relay ramps, folding and secondary faulting in detail. Modelling can be used at any scale, from lithospheric scale showing the formation and evolution of orogenesis to a smaller scale showing the growth and linkage of faults and fractures.

Analogue models have been carried out through time to imitate and to get a better understanding of how faults evolve with time and space. A range of different approaches have been developed over time, with the most common setups using clay, (e.g. Reches (1988), Ackermann et al. (2001) and Henza et al. (2010)), sand, (e.g. Buchanan and McClay (1991), McClay and Scott (1991) and McClay and White (1995)) and plaster, (e.g. Sales (1987), Fossen and Gabrielsen (1996) and Mansfield and Cartwright (2001)) as the modelling material. The modelling material can either be used alone or in combination with barite and silicone which correspond to the ductile lower crust (Brun et al., 1994).
Deformation related to salt tectonics covers a wide range of structures. Analogue models of salt tectonics and related structures have been made by Vendeville and Jackson (1992) and Schultz-Ela et al. (1993).

Previous studies of analogue models show that structures reproduced in the laboratory are very similar to those observed in natural rocks (Fossen and Gabrielsen, 1996, Schlagenhauf et al., 2008). Analogue models have been made of the Outer Moray Firth basin, Viking Graben and San Andreas Fault among others.

3.2 Early experimental work in structural geology

Physical analogue modelling of faulting has been done by geologists for more than a century to simulate deformation and tectonics of the upper crust. The first experimental models tried to reproduce folds observed in mountain ranges. In 1815, Sir James Hall was the first geologist to develop a model to explain the origin of folds. The model was made up of a thick

series of pieces of cloth stacked vertically. The model was compressed horizontally between two wooden boards, which resulted in folding of the cloths. In 1878, Gabriel Duabrée studied the influence of rheology and layer thickness of a single layer fold by using a wooden box equipped with a worm screw to deform layers of zinc, iron or laminated lead. His result showed that the fold's wavelength depends on the thickness and rheology, whereas the symmetry depends on the confining pressure (Graveleau et al., 2012).

One of the first geologists that investigated mountain building was Cadell (1888). His models showed fold and thrust faulting in a contractional regime inspired by his observation from the Scottish Highlands. Thin layers of dry plaster powder interbedded with thicker layers of wet sand were used. When the plaster had absorbed enough moisture from the sand, it deformed brittle, and faults formed when stress was applied (Cadell, 1888).

Mead (1920) did one of the first analogue experiments with extension. He used a frame with one rigid clamp at one end, and a moveable clamp at the opposite side. Tension fractures developed by stretching a rubber sheet fastened at the edge of the two clamps. The rubber sheet was then covered with paraffin, and when the paraffin had become brittle, the rubber sheet was exposed for further stretching, and a set of tensile fractures occurred (Mead, 1920). Cloos (1955) continued to work with extension models by using clay as a modelling material. He is also one of the first geologists considering and applying scaling of materials based on Hubbert (1937) statements. The experiments were performed on a moveable square of wire cloth, which was pulled diagonally, and joints opened perpendicular to the pull direction (Cloos, 1955).

3.2.1 Clay models

Clay is one of the most common materials used in modelling of faults throughout time. The deformation of wet clay in response to applied stress occurs in the same way as for natural rocks. The wet clay used in modelling of faults usually consists of kaolinite, and the particle size is less than 5μm. The clay normally has a weight ratio of 40 % water (Ackermann et al., 2001, Henza et al., 2010). Due to the clay's high water content it also has a cohesive strength. The faults formed in clay models are narrow and well defined due to the grain size. The grain size also reflects the number of major and minor secondary faults formed in the model, which increase with extension rate (Eisenstadt and Sims, 2005). In general, the deformation is more distributed in clay models with several major and minor faults in addition to folds compared to sand model.

More recent work with clay has been done by Ackermann et al. (2001) who studied how normal fault systems evolve with increasing strain, and the influence of mechanical layer thickness in different models. Henza et al. (2011) used scaled analogue models to see how pre-existing extensional faults affect fault reactivation in a second phase of extension with an oblique angle of 45^{o} to the first phase of extension. (Henza et al., 2011).

3.2.2 Sandbox models

Together with clay, sand is one of the most common materials used in analogue modelling of faults. The sand usually consists of quartz sand and the average grain size varies from 190 μm (Keep and McClay, 1997), 300μm (Buchanan and McClay, 1991) and up to 700μm (McClay and Ellis, 1987) in different experiments. Previous testing of the sand's mechanical properties has shown that its internal angle of friction is 31^{o} (McClay and Ellis, 1987, Buchanan and McClay, 1991). There is a correlation between grain size and fault width. Due to a relatively coarse grain size, sand used as a modelling material gives wider fault zones compared to clay and plaster. The deformation structures are located in a few major faults in sand models, whereas in clay the deformation is distributed over a wider area and in several major faults, minor faults and folds (Henza et al., 2010). In addition small-scale structures related to faulting are not well-represented compared to clay and plaster models that give more small-scale discrete structures. Faults propagate and link rapidly in sand compared with wet clay. Also the displacement along individual faults in sand is greater than in clay because the sand has a lower cohesive strength (Eisenstadt and Sims, 2005).

Sandbox experiments are usually done by using interbedded sand layers with two different colors to record the displacement during increasing deformation. McClay (1990) used sand to simulate brittle structures found in the upper 10 km of the crust. Analogue models with sand have also been used to study the evolution of relay structures (Hus et al., 2005), pull-apart basins in releasing stepovers (Wu et al., 2009), listric faults (Buchanan and McClay, 1991) and the influence that the detachment has on the hanging wall deformation (McClay and Scott, 1991).

3.2.3 Plaster models

Plaster is a less common used material in analogue models, but has successfully been used by e.g. Sales (1987), Fossen and Gabrielsen (1996) and Mansfield and Cartwright (2001). The fine grain size of plaster, rapid transition from liquid to solid state and durability makes plaster a suitable modelling material. Major faults and minor antithetic and synthetic faults and fractures are well developed. The fault zones are narrow, and small-scale deformation

structures are well reproduced (Fossen and Gabrielsen, 1996). Models can also be preserved for further studies and analysed in addition to pictures. The physical properties of plaster depend on the plaster water ratio. Therefore, the strength and density of the plaster water mix increases with decreasing amount of water in the mixture.
The physical properties of plaster make it suitable for dynamic experiments. The high compressive strength compared to tensile strength and the low tensile strength of plaster result in only a low force being required to deform the plaster (Coffin and Kumar, 1964).

Sales (1987) made analogue models for both strike-slip, extension and contraction regimes by using plaster of Paris. Fossen and Gabrielsen (1996) made extensional models, showing that major faults are composite features that vary along dip from single faults to complex fault zones. The main fault accommodates 60 -70 % of the deformation, while minor smaller faults only account for 10 – 20 %. Mansfield and Cartwright (2001) focused on the accumulation of displacement and length with growth and linkage of fault segments.

CHAPTER 4 – METHODOLOGY

4.1 Introduction

This chapter describes analogue modelling techniques used in this study. The modelling materials are described, in addition to the advantages and disadvantages of using plaster of Paris as a modelling material in analogue experiments. A review of the experimental set-up and procedure is also presented. In the end, there is an explanation of quantitative methods used for this thesis including ArcGIS. ArcGIS is used to analyse pictures from different experiments to investigate and quantify the connectivity/topology of the modelled fault and fracture networks. A summary of the workflow is illustrated in Fig. 4.1.

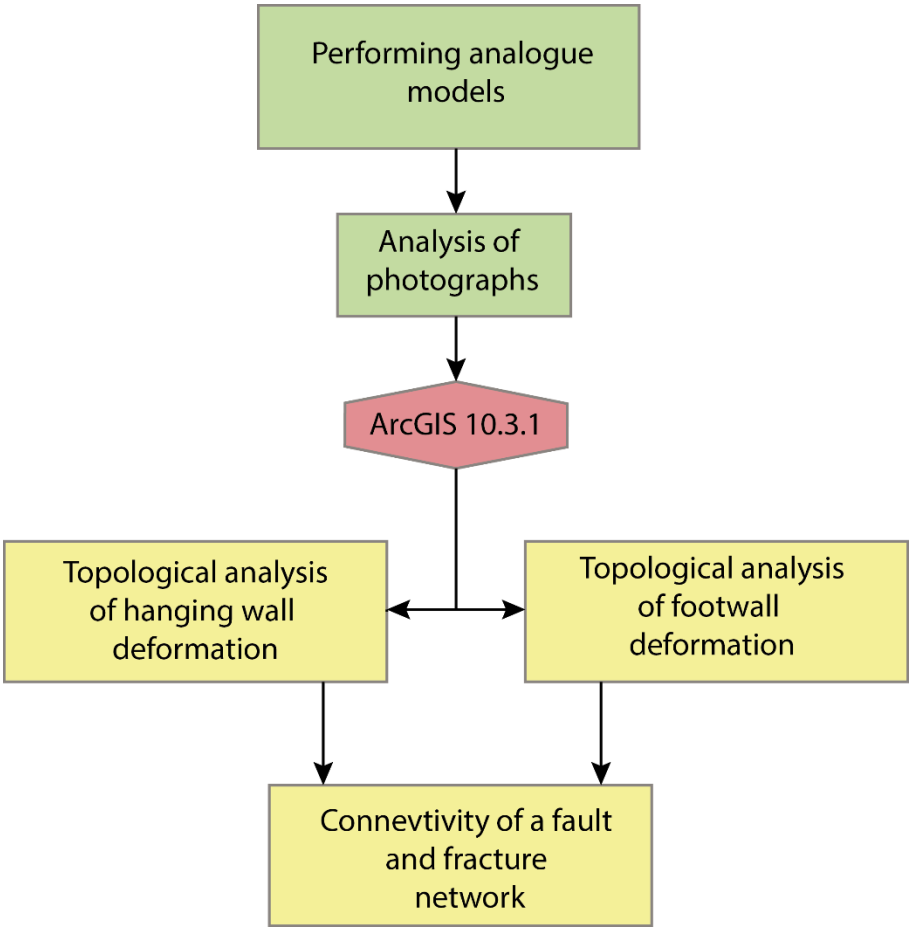

Fig. 4.1: Flow chart illustration the workflow for this thesis. Green represents experimental work and analysing of photos, red is work in Arc GIS 10.3.1 and yellow is the outcome from the analysis of photos in ArcGIS 10.3.1.

4.2 Plaster of Paris

The type of plaster used in experiments in this thesis is "Molda 3 normal". Plaster of Paris ($CaSO_4$ x ½ H_2O) is produced by partial dehydration of gypsum where three quarters of the water content are removed due to heating (equation 4.1).

$$CaSO_4 \times 2\ H_2O + \text{heat} \rightarrow CaSO_4 \times ½\ H_2O + 1½\ H_2O \quad (4.1)$$

The plaster type consists of at least 91 % pure gypsum, and 97 % of the grains are less than 100 μm, and the remaining 3 % are less than 200 μm (Saint-Gobain, 2015). The volumetric plaster water ratio used in each experiment is 1.7:1. The final setting time of the plaster is 39 minutes (Saint-Gobain, 2016).

4.2.1 Advantages with plaster as modelling material

There are several reasons for choosing plaster as a deforming material in analogue models in addition to the simple set-up and performance. The main advantage by using plaster as a modelling material is the durability of solid models that can be preserved for further analysis, in addition to pictures. Due to the fine grain size of plaster particles, the faults created are narrow, and produce a wide range of faults and fractures compared to sand as a modelling material (Mansfield and Cartwright, 2001). The wide range of faults gives the opportunity to study the relation between the major faults and minor synthetic and antithetic faults in each experiment (Fossen and Gabrielsen, 1996). Plaster of Paris has a low modulus of elasticity and low tensile strength, and thus requires relatively small forces for brittle deformation to occur.

4.2.2 Disadvantages with plaster as modelling material

Even though there are several reasons for choosing plaster of Paris as the deformation material, there are also some disadvantages, as with any other modelling material. Materials used in the experiments have to be scaled down from km scale in the nature to cm scale in the model. Plaster has a relative high cohesive strength compared to natural rocks when it is scaled down (Ellis and McClay, 1988). This means that an almost cohesion-less material is best suited for the model in theory.

The properties of the plaster change during the experiment as it solidifies (Fossen and Gabrielsen, 1996). This may have an effect on the deformation mechanisms and structures related to faulting. The viscosity of the plaster should be the same for each experiment to compare the different models, however this is not the case as the rheology of the plaster

changes with time. A film of water separated from the plaster may develop at the top of the plaster if it is poured into the deformation box before it has become viscous enough. This water film may have an influence on small scale structures which develop at the surface during deformation.

As with any other types of analogue experiments, frictional drag along the sidewalls of the deformation rig will occur, resulting in edge effects along the sidewalls. Another limitation is that the plaster used in these analogue experiments are homogenous, whereas in the lithosphere there are stratigraphic layers which react differently to applied stress and temperature, and will therefore not deform homogenously, but differently for each layer.

4.3 Barite

A mix of barite ($BaSO_4$) and water is used as a basal layer during each experiment. The barite and water mix has a higher viscosity than the liquefied plaster, and deforms in a ductile manner. The viscosity can be decreased with increasing amount of water. The barite does not solidify, and can be reused several times. Two variations of the basal layer are used in this thesis; horizontal and wedge shaped. The different variations of the barite result in different fault geometry of the plaster during deformation. This was done to develop more than one main fault in the models.

4.4 Experimental set-up and performance

The experimental set-up is similar to the one used by Mansfield and Cartwright (2001). The experiment is performed in an open top wooden box with four rigid walls and a moveable internal wall. The dimensions of the deformation rig are 45x45x15 cm (Fig. 4.2). A worm screw with a handle in the end connects the internal moveable wall with the rigid wall. By cranking the handle, the internal wall moves.

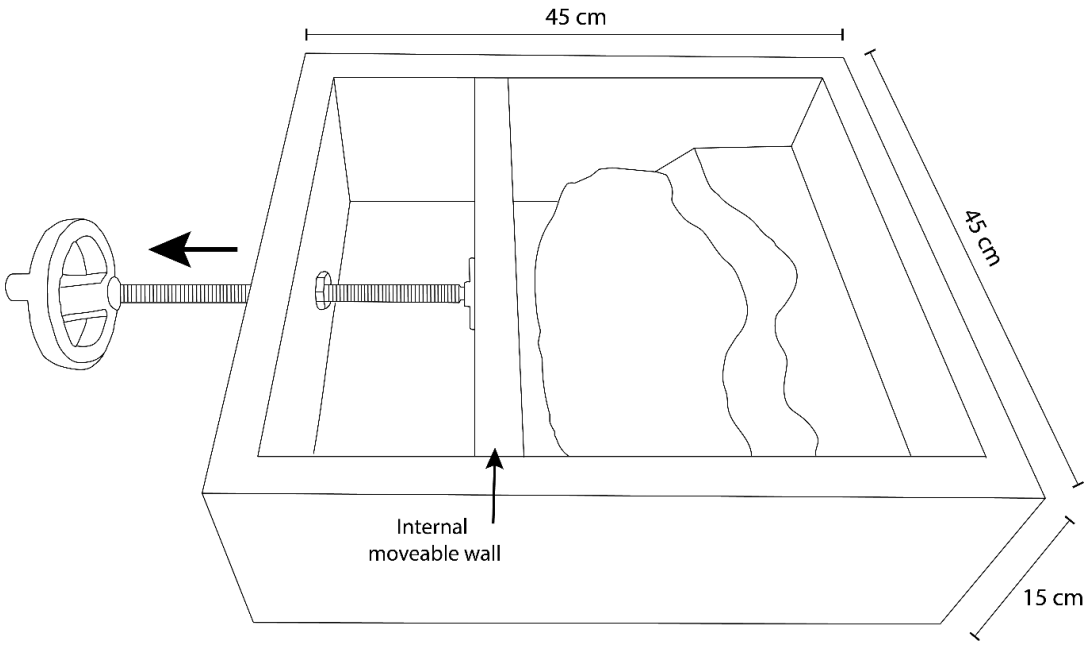

Fig. 4.2: A schematic illustration of the deformation rig used for each modelling experiment. The plaster of Paris and barite were layered in approximately half of this box.

Before each experiment, the sidewalls of the deformation rig are covered with canola oil to reduce friction, and to make it easier to remove the plaster model after the deformation. Barite is smeared at the base of the box, along the short wall in the back and in the corners to prevent leaking of liquefied gypsum. The thickness of the barite layer at the base of the deformation box varies between different experiments (usually around 1 cm or wedge shaped). The plaster is then poured into the box when it is still liquid. To check if the plaster is stiff enough, a screw is used to make a small mound in the plaster mix. If the mound keeps its shape for a short period of time, the plaster is stiff enough to deform by brittle failure during extension. By moving the internal wall, the plaster deforms under gravitational collapse, producing an evolving array of extensional faults and fractures.

Good lighting during each experiment is important to take high quality photos that show the growth and linkage of faults at the surface. This is achieved by two lights fastened to the wall pointing toward the model. Another two handheld lamps are used in addition to get the surface structures cast additional shadows.

4.4.1 Documentation of experiments

The experiments were documented by three Nikon D800 digital SLR cameras with an AF-S Nikkor 50 mm f/i.4 G lens. One camera is attached to the ceiling taking pictures from top-down. The other two cameras are placed at each side of the model with a high angle to the

model. This way, the cameras capture the model from different angles. During the experiment, four photos were taken per second.

Close-up photos were taken after each experiment to document small- and large scale structures in each model. In addition, photos are combined to create videos of the experiment. This way, the entire experiments can be viewed numerous of times when analysed. These videos are found as attachments to this thesis.

4.4.2 Calculation of extension

The calculation of total extension is based on the initial length of the different models:

$$\varepsilon = \frac{L - L_0}{L_0} \text{ x } 100\% \quad (1)$$

Where

ε = Amount of extension in %

L = Amount of extension in cm.

L_0 = Initial length, cm.

One experiment presented reached over 100 % extension while the rest of them reached somewhere between 60-90 % extension. The average extension rate has been calculated based on the time signature provided by the cameras from each experiment:

$$\dot{\varepsilon} = \frac{\varepsilon}{t} \quad (2)$$

Where

$\dot{\varepsilon}$ = Average extension rate

ε = Elongation (mm)

t = Time (seconds)

4.5 Scaling

Analogue models made in the lab attempt to simulate processes that operate on scales ranging from centimetres to 10s to 100s of kilometres in nature, and must therefore be scaled down to be a representable model. The mechanical properties of materials used in analogue models should be scaled to the mechanical properties of natural rock in order to make an ideal representation (Hubbert, 1937). The similarity between the nature and analogue model can be described by three criteria;

1. Geometrical similarity is achieved when all corresponding angles between two bodies are equal and the corresponding lengths are proportional.
2. Kinematic similarity applies when two geometrically similar bodies are exposed to similar changes in shape and/or position.
3. Dynamic similarity is achieved when the model is both geometrically and kinematically similar, and the ratio between the mechanical forces acting on equivalent particles in the model and the prototype are constant (Koyi, 1997). The model requires similar mass distribution as the natural rock (Hubbert, 1937). When the ratio between mass and length of two bodies of different size is scaled, the density is obtained directly.

Geometrical symmetry is relatively easy to achieve by scaling the model down to the prototype. Physical scaling, which includes kinematic and dynamic similarity is more complex. Variables that characterise the model (e.g. time, velocity, density, viscosity and length) must be proportionally scaled from the natural rock (Ranalli, 2001). This means that if the size is decreased, so must the strength of the used material for analogue models. According to Fossen and Gabrielsen (1996) scaling of different materials can be challenging. Dry sand is a cohesion-less material, whereas the cohesive strength of the plaster is too high when it is scaled to nature. In addition, when scaling the grain size to plaster it become too large (~10 cm if it is scaled down from 1 km) and unrealistic compared to natural rocks.

4.6 Quantitative methods

4.6.1 Topology

ArcGIS is a geographical information system (GIS), used for management, analysis and display of geographical data. In this thesis, ArcGIS has been used for topological analysis of fracture networks of three different models, 5, 11 and 13. These models have been subjected to a detailed analysis with regards to the topology (Fig. 4.3) of fracture networks, and thus the connectivity in analogue models. For each model, three photos with increasing amounts of

strain have been interpreted. The result from the analysis is shown in triangular plots of node and branch proportions. The topology of fault and fracture networks was obtained by using the spatial relation feature in ArcGIS and excel.

In ArcGIS, nodes, branches and slip surfaces are organised into different feature classes. Feature classes are collections of features of the same type. For example, I-nodes create one feature class and I-C branches make up another class. Nodes, which mark fault tips and intersections where faults abut or cross are marked as points. Branches define faults and fractures and are represented by polylines. Fault planes are highlighted as polygons. Two sample areas are defined, one in the footwall and the other one in the hanging wall. These areas are defined by the extent of faults and fractures.

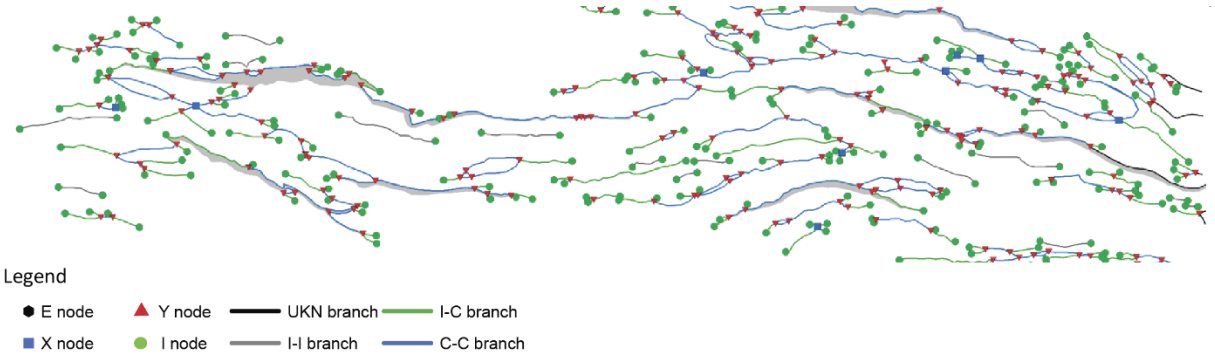

Fig. 4.3: Example of a sketched map for topological analysis of a fault and fracture network of model 11-15. The sketched map shows just a section of the model, and is from the final deformation stage. The grey areas are the slip surfaces.

4.6.2 Connectivity

The interpretation of the fault and fracture network in each model is used to make contour maps of connecting node frequency (N_C/mm^2) and branch intensity (mm/mm^2). These contour maps show the evolution of the connectivity in each model during the deformation process. Contour maps of connecting node frequency are made by merging of connecting nodes (Y-nodes and X-nodes) which gives a new point feature class. The new feature class with connecting nodes is put into "Kernel density" which is a tool for calculating the density of features, in this case connecting nodes per square millimetre.

The branch intensity is measured as the total branch length within a square millimetre. This is done by the same method as connecting nodes, expect all types of branches are merged together to quantify the intensity. This results in a contour map of branch intensity. The output

cell size used is 0.5 mm and the search radius is 10 mm around each feature in the different models.

The total number of different nodes and branches, and the total trace length within the sampling area is summarised. The properties of a fracture network can be classified depending on the proportion of different nodes. To visualise the classification, excel has been used to plot the network properties in a triangular diagram, showing the proportion of I, Y and X nodes, and I-I, I-C and C-C branches (Fig. 4.4). In the triangular plots the numbers 0 – 2.0 represent the average number of connections per branch. In the theory, the average connections per branch should cluster around the curve in the branch plot. Connectivity in different systems can be measured by the value of the average number of connections per branch (C_B).

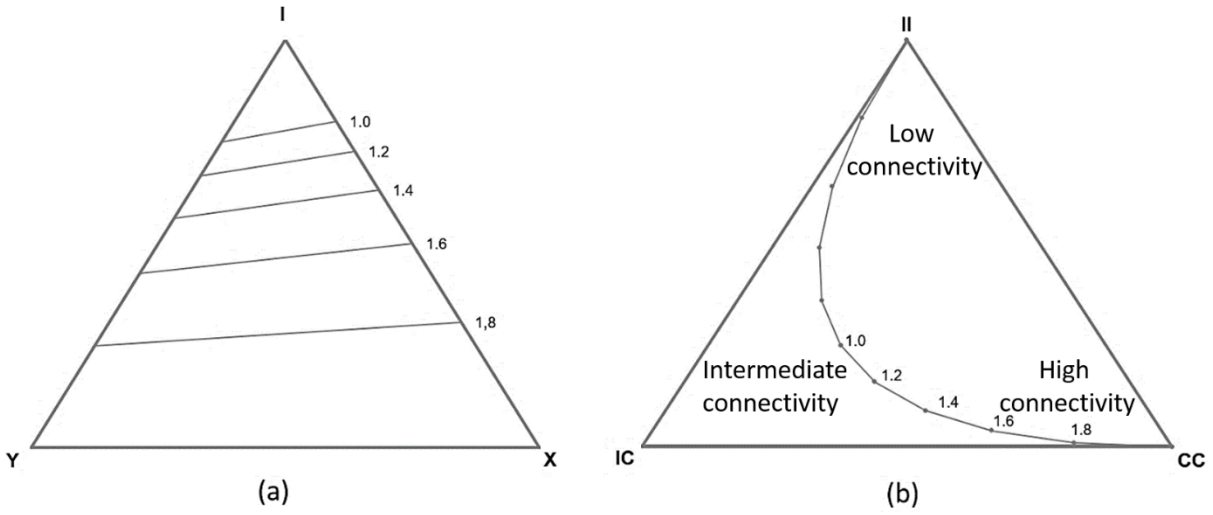

Fig. 4.4: (a) Triangular plot of node proportion. (b) Triangular plot of branch proportion. The numbers 0 - 2.0 indicate the average connections per branch.

4.6.3 Fault measurements

The faults used to analyse the displacement length ratio were those that did not intersect with the walls of the deformation rig, and were not influenced by edge effects. This means that the chosen faults had free tips. No major faults are therefor used in the analysis, as they all were cutting across the whole model or intersected with one wall.

The length measurements of faults are done on a millimetre scale and recorded along the fault plane between two well defined fault tips. These measurements are recorded in photographs from four different stages with increasing strain. Different faults are chosen for the measurements, both the ones that intersect and connect, and faults that grow along a single fault plane.

The displacement is defined as the dip-slip displacement of the surface, and was recorded from the photographs using illustrator and a millimetre scale. The result is based on measurements of the same fault in four different photographs with increasing extension.

CHAPTER 5 – RESULTS

5.1 Introduction

A total of 20 experiments were conducted in the lab for this thesis. Of these, six experiments were selected for further analysis (*Table 5.1*). The selection of experiments was based on the photo quality and the types of structures found in the models where the evolution can be studied in detail. Some of the models show a simple evolution with one main fault, whereas other shows a more complex fault system involving several major faults. A stepwise illustration of the evolution of the fault system is made to give the reader a better understanding in addition to attached videos, and is found after the description of the evolution pathway.

The results presented will focus on the evolution of faults and fault-related deformation in the hanging wall and footwall over time. In all models the first major fault to develop is marked as F1, the second one F2, and so on. Antithetic faults and fractures are marked in red and synthetic fault and fractures are marked in black.

For three of six experiments (model 5-15, 11-15 and 13-15), results from the topological analysis and contour plots of connecting node frequency and branch intensity are presented after the description of the experiments. The connecting node frequency and branch intensity from the contour plots and from the excel sheet are not the same. The numbers from excel are much lower than the legend of the contour plots. The reason is that the contour plots are focusing on smaller areas for each cell, they describe has subareas of more intense deformation.

Table 5.1: Overview of the experiments presented in the results chapter

Experiment number	Basal layer	Initial length	Final length	Mean extension rate ($\dot{\varepsilon}$)	Total extension
5-15	Horizontal barite	16.5 cm	29 cm	10.0 mm/s	63 %
7-15	Horizontal barite	16.5 cm	28.5 cm	9.8 mm/s	88 %
11-15	Horizontal barite	17 cm	29.5 cm	8.4 mm/s	73.5 %
12-15	Wedge shaped barite	17 cm	35 cm	8.9 mm/s	106 %
13-15	Horizontal barite	16.5 cm	28.5 cm	11.4 mm/s	73 %
19-15	Wedge shaped barite	15 cm	29 cm	9.6 mm/s	93 %

5.2 Description of experiment 5-15

A stepwise evolution of the deformation throughout the experiment can be followed in figure 5.2. General information about the setup and duration of experiment 5-15 is found in table 5.2. A video of the experiment is found in Appendix A.

Table 5.2: General information about the setup and duration of experiment 5-15

Date	22.10.2015
Water plaster ratio	1:1.7
Basal layer	Horizontal barite layer (1 cm thick)
Initial length	16.5 cm
Final length	29 cm
Total displacement	12.5 cm
Total extension	63 %
Duration	29 seconds
Mean extension rate ($\dot{\varepsilon}$)	10 mm/s
Notes	Pictures from the first 3.5 cm of deformation are missing from the top camera. The fractures are harder to observe from the oblique view cameras, and there is therefore a higher uncertainty when the first fractures develop in this model.

0 – 21 % extension

Fractures start developing in the model after ~15 % extension, and become better defined with increasing extension. The fractures develop perpendicular to the stretching direction, i.e. with an E-W orientation. At the end of the deformation history, some of the fractures have developed into minor fault segments. These fractures grow via sympathetic increase of length and displacement. The highest density of fractures is located to the west in the model at the end of this stage.

21 – 30 % extension

The isolated fault segments grow along strike and in slip direction as the extension increases. Two main fault segments (F1 and F2) developed in this model. These faults grow by linking up with adjacent minor faults, and show a sympathetic increase of length and displacement. A relay ramp develops in the central part of the model between fault segment F1 and F2 after

24 % of extension. The relay ramp is only present for about 6 % of the extension before it breaches. The breaching of the relay ramp is a so-called “single tip” footwall breach where the relay ramp is partly preserved in the hanging wall. This happens due to accommodation of displacement in F1 and F2, and the development of minor E-W orientated fractures at the ramp. The breaching of the relay ramp results in the development of a through-going fault plane, F1’, across the model. A minimum displacement is located in the linkage area of F1 and F2 and the through-going fault typically has a curved geometry in the linkage area.

30 – 51 % extension

Fractures start to develop close to the internal moveable wall with increasing extension. As the extension continues, new faults and fractures develop in the hanging wall to F1’ in addition to growth of established minor fractures. South of the linkage area of F1 and F2, an area with higher fracture density has developed. In the western part of the model, two minor faults, F3 and F4, develop. These faults are soft-linked fault segments connected by a relay ramp. F3 grows during sympathetic increase of length and displacement while F4 has a more rapid establishment of its length, and accommodates displacement with only minor tip propagation. F3 and F4 are subparallel overlapping fault segments with an approximately E-W orientation. The area between the fractured area in the central part of the model and the faults to the east are more or less undeformed at the end of this stage.

51 – 63 % extension

The major fault F1’ is active until the deformation reaches 57 %. This means that F1’ has been active over 27 % of the extension.

An array of isolated fractures develops in front of the F4 fault tip. As the extension increases, these isolated segments grow via sympathetic increase of length and displacement, and link up with one another by curving toward the opposite fault. This results in characteristically curved linked fault segments. At the same time, the relay ramp connecting F3 and F4 breaches, creating F3’. Splaying faults can be observed near the termination of some of the linked fault segments. As for the rest of the model, E-W orientated fractures develop toward the last part of the deformation history. The highest fracture density is located in the hanging wall of F1’ in front of the linkage area of F1 and F2.

The fault activity from model 5-15 is summarised in figure 5.1. Fault F3 and F4 develops in the hanging wall to F1', when it still accumulates slip. The linkage of F3 and F4 occur when the main fault is less active, and most of the displacement is accommodated in hanging wall structures.

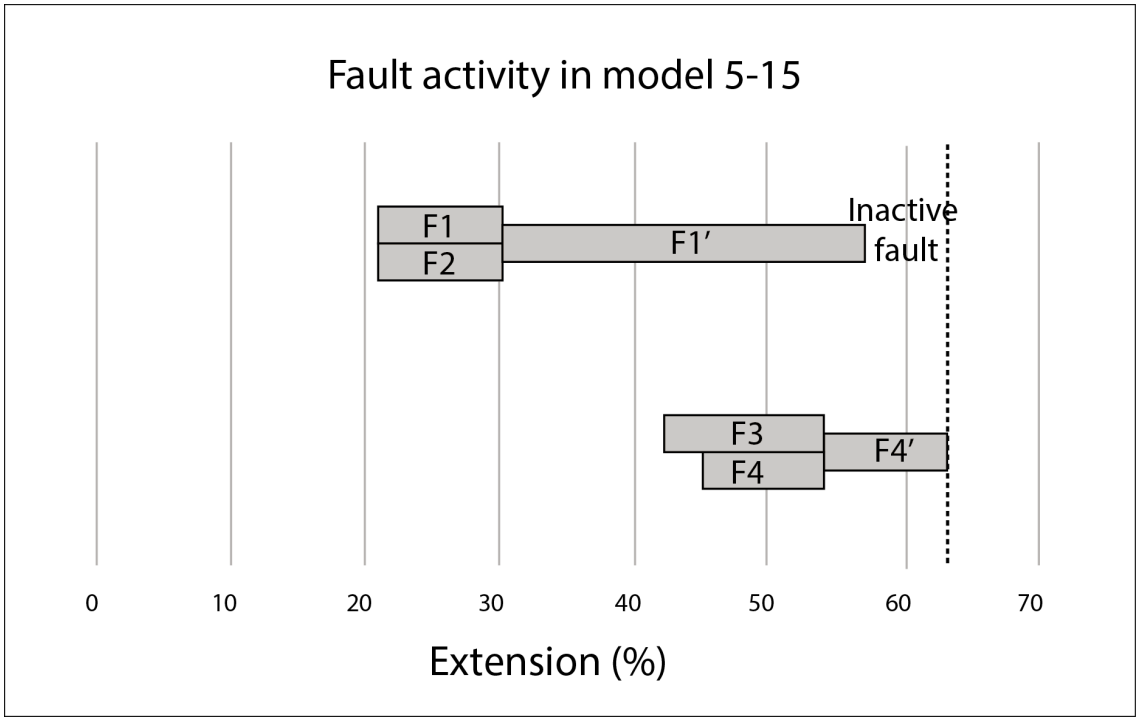

Fig. 5.1: Diagram, which summarises the evolution and activity of the major faults during the extension in model 5-15. The fault number is marked in the bars. The total extension in this experiment is 63 % and is indicated with a dashed line. Faults which link up to develop longer faults are clustered together.

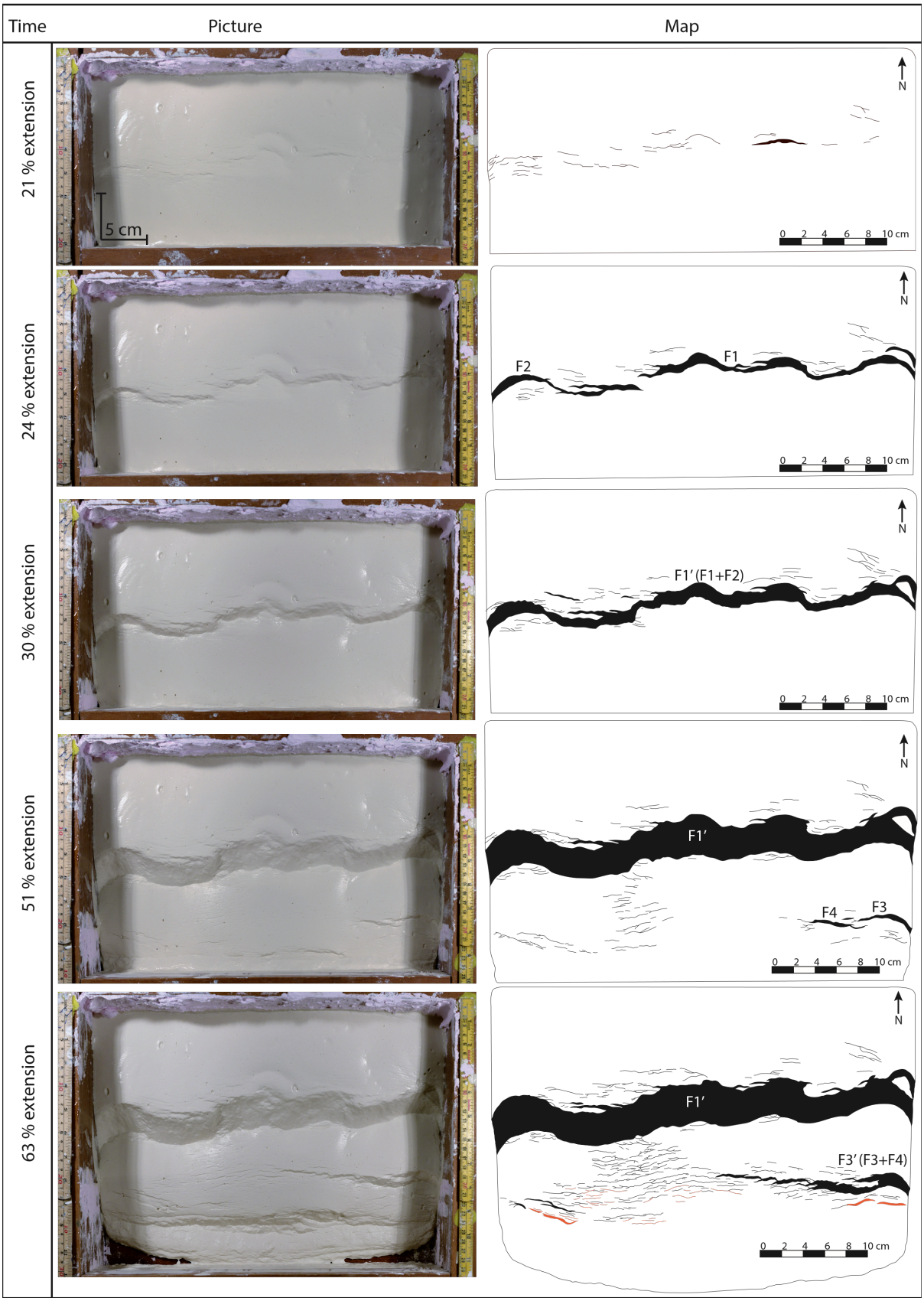

Fig. 5.2: The structural evolution of model 5-15 seen in map view. The black lines and fields represent synthetic fractures and heave. The red lines and fields represent antithetic fractures and heave. Image to the left and line drawings to the right.

Topology of fracture network in model 5-15

The topological analysis of model 5-15 shows the evolution of the fault and fracture network after 30 %, 45% and 63 % of the total extension. These measurements show that the connectivity is greater in the footwall than in the hanging wall at the early stage of extension. With increasing strain, faults and fractures continue to develop in the hanging wall, whereas little change is seen in the footwall. The evolution of the connectivity in both the footwall and hanging wall is shown in triangular plots. The triangular plots show that the proportion of nodes and branches in the footwall only shows a slight increase with increasing extension. In the hanging wall on the other hand, there is a larger increase in connectivity.

The triangular plot of node proportions (Fig. 5.3a) shows that the proportion of I-nodes is as high as 87 % after 30 % of extension in the hanging wall. As the strain increases, the proportion of Y-nodes increases at the expense of a decrease in I-nodes. The amount of X-nodes slightly increases as it goes from 0 to 2 %. The proportion of I-nodes after the deformation is 54 %. In the footwall, there is less change in node proportion with increasing deformation. The proportion of I-nodes changes from 58 % to 48 %. A decrease in I-nodes results in an increase of Y-nodes. The proportion of X-nodes remains constant during deformation.

The triangular plot of branch proportions (Fig. 5.3b) shows that the average connections per branch in the hanging wall increase from around 0.9 to 1.4 with increasing strain. This means that the model develops from consisting of mostly I-I and I-C branches to a gradually higher proportion of I-C and C-C branches, whereas the proportion of I-I branches decreases from 28 % to 7%. In the footwall on the other hand, the average connections per branch change from 1.3 to 1.5 with increasing extension. The proportion of I-I branches only shows a slight change (from 9 % to 6 %), whereas the proportion of I-C branches decreases as the proportion of C-C branches increases with strain. The majority of these changes occur between 30 - 45 % of the total extension.

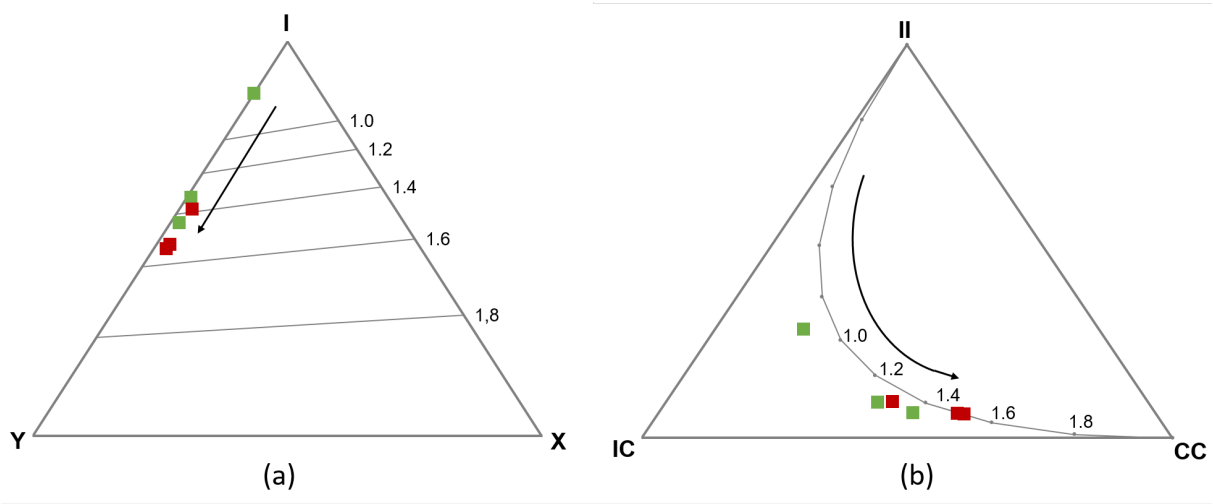

Fig. 5.3:The green and red points are measurements from the hanging wall and footwall, respectively. The arrows show the evolutionary path from a simple network to a more complex one. The numbers 1.0 - 2.0 are numbers of connections per branch (CB). These measurements are from the footwall and hanging wall of F1'. (a) a triangular plot of node proportion. (b) a triangular plot that shows the proportion of different branch types.

Contour plots of connecting node frequency (Y-nodes and X-nodes) and branch intensity are used to assess the connectivity in a fault and fracture network (Fig. 5.4). These plots give the spatial distribution of topological features. The branch intensity (mm/mm^2) varies from 0.02 to 0.09 mm/mm^2 in the hanging wall and from 0.11 to 0.14 mm/mm^2 in the footwall during the deformation process. Areas with a high branch density usually consist of several small fractures that interact, whereas areas with a lower fracture density usually consist of longer branches. The connecting node frequency varies from 0.002 to 0.013 N_C/mm^2 in the hanging wall and from 0.013 to 0.015 N_C/mm^2 in the footwall, indicating that the areas with best connectivity are located in the footwall. Maxima with connecting node frequency and the branch intensity coincide. This indicates that the connecting node density is related to areas with high fracture intensity.

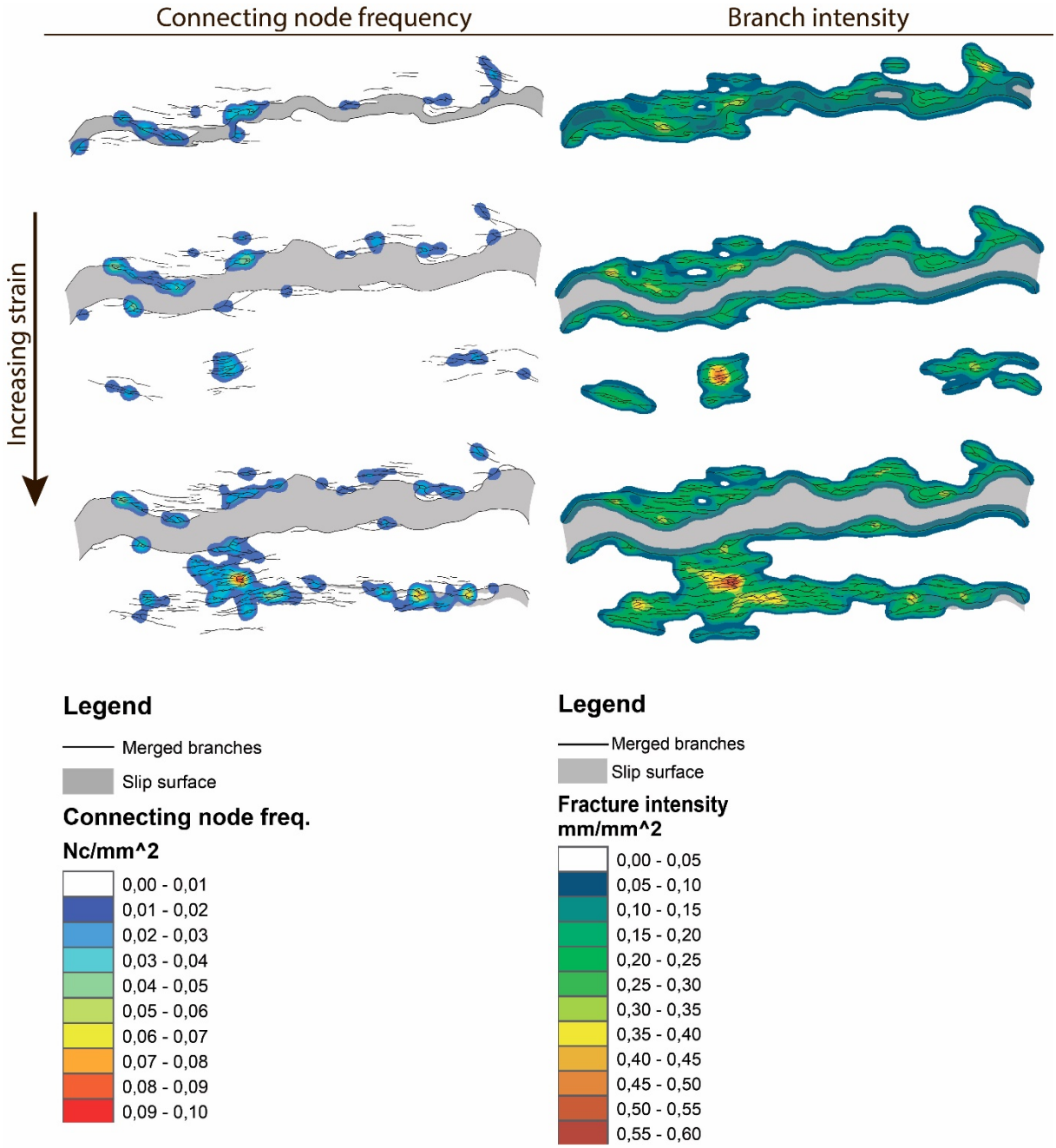

Fig. 5.4: Contour plot of model 11-15 showing the connecting node frequency (left) and branch intensity (right). The three different stages show the evolution of the connectivity with increasing strain. The measurement of the connecting node density is calculated from the number of connecting nodes (N_C) per mm^2, whereas the branch intensity is calculated from the total branch length (mm) per mm^2.

5.3 Description of experiment 7-15

A stepwise evolution of the deformation throughout the experiment can be followed in figure 5.5. General information about the setup and duration of experiment 7-15 is found in table 5.3. A video of the experiment is found in Appendix A.

Table 5.3: General information about the setup and duration of experiment 7-15

Date:	22.10.2015
Water plaster ratio:	1:1.7
Basal layer:	Horizontal barite (1 cm thick)
Initial length:	16.5 cm
Final length:	28.5 cm
Total displacement	12 cm
Total extension	88 %
Duration	29 seconds
Mean extension rate ($\dot{\varepsilon}$)	9.8 mm/s

0 – 21 % extension

Fractures start developing in the model after ~13 % extension. Some of these fractures develop into minor faults with increasing extension, and grow via sympathetic increase of length and displacement. These early developed faults, F1 and F2, are located in the central part of the model with an orientation NW-SE. An area with high fracture density develops to the west in the model. In this area with a high fracture density, minor faults develop with increasing strain, resulting in F3 and F4. After 21 % extension, four main fault segments have developed across the model. F1 and F2, and F2 and F4 are soft linked, resulting in relay ramps connecting the hanging wall and footwall to the different faults. In the eastern part of the model, two areas with increased density of fractures compared to the surroundings have developed. The area furthest to the south has an orientation NW-SE, while the area to the north have a predominantly NE-SW orientation.

21 – 30 % extension

The two areas with a high fracture density to the east in the model continue to evolve with increasing strain. In the area to the north, fractures link up and eventually, several minor faults develop. The area to the south is more strongly dominated by sympathetic growth of fractures, resulting in faults displacement is accumulated, and the development of fault segment, F5.

Both F3 and F4 grow along strike as displacement is accommodated, and eventually intersect. The faults continue to grow as the strain increases, which results in breaching of the relay ramp between F2 and F4. In addition, curving of fault F1 toward F2 results in breaching of the relay ramp between fault F1 and F2. The breached relay ramp is partly preserved in the hanging wall. The hard linkage between F1 and F2 results in the development of F1'. After the development of F1', a minimum displacement of the fault is located in the linkage area, and the fault plane has a curved geometry. F1' and F5 overlap at the end of this stage and a new relay ramp develops.

30 – 50 % extension

The isolated fault segments in the NE corner of the model grow along strike and in slip direction as the strain increases, and eventually link up with one another and abut against F1'. Breaching of the relay ramp connecting F1' and F5 results in linkage of these fault segments and the development of a through-going fault plane across the model with an E-W orientation. The minimum displacement in the model is in the linkage area between F1' and F5 at this point. Most of the deformation in the hanging wall occurs toward the end of this stage. Fractures start to develop close to the internal moveable wall and close to the slip surface to F1', mainly south of the linkage area of the different fault segments at an earlier stage.

50 – 88 % extension

In the early part of this stage, most of the displacement is accommodated by the major fault, F1'. As the intensity of fractures and minor faults in the hanging wall to F1' increases, F1' accommodates less displacement, and becomes inactive after 72 % extension.

Fractures with an orientation approximately N-S develop in the eastern part in the footwall to F5. The hanging wall deformation is mainly located to the west and the central part in the early stage and both synthetic and antithetic fractures develop at the same time. The orientation of the fractures and minor faults are E-W. Some of the fractures grow by a sympathetic increase of length and displacement, whereas others show a rapid establishment of the length with only minor tip propagation as the displacement is accommodated. With increasing extension fractures develop in the eastern part of the hanging wall and link up to form minor faults. Areas with linkage of fault segments and breached relay ramps have a curved geometry in the linkage area. Horst and graben structures have developed at the end of this stage across the model. The most defined structures are located in the central part of the hanging wall to F1'.

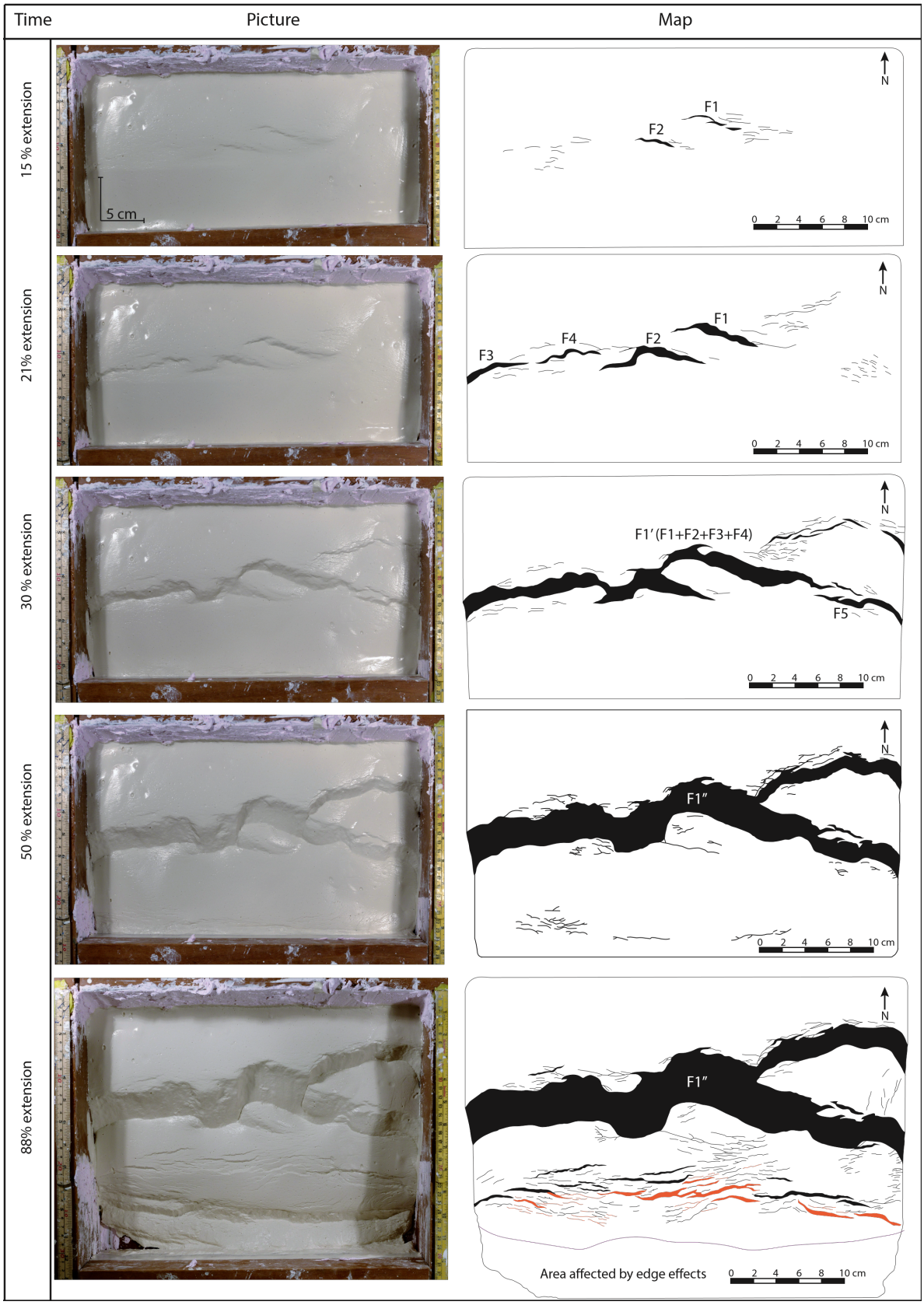

Fig. 5.5: Structural evolution of model 7-15 seen in map view. The black lines and fields represent synthetic fractures and heave. The red lines and fields represent antithetic fractures and heave. Image to the left and line drawings to the right.

5.4 Description of experiment 11-15

A stepwise evolution of the deformation throughout the experiment can be followed in figure 5.6. General information about the setup and duration of experiment 11-15 is found in table 5.4. A video of the experiment is found in Appendix A.

Table 5.4: General information about the setup and duration of experiment 11-15

Date:	22.10.2015
Water plaster ratio	1:1.7
Basal layer	Horizontal barite
Initial length	17 cm
Final length	29.5 cm
Total displacement	12.5 cm
Total extension	73.5 %
Duration	35 seconds
Mean extension rate ($\dot{\varepsilon}$)	8.4 mm/s
Notes	The plaster volume was not constant through the whole experiment. The volume loss during the experiment is approximately 50.4 cm^3. Pictures from the top camera are missing between 25-27 cm.

0 – 26.5 % extension

Fractures start developing after ~15 % of the total extension. The majority of these early-developed fractures are located at each side of the model with an undeformed area inbetween. The fractures have an oblique angle to the sidewalls of the model. As the strain increases, fractures link up, and minor faults develop creating a fault array with approximately the same strike. Some of these isolated segments are connected by small relay ramps. The deformation in the central part of the model occurs toward the end of this stage. Moreover, there are still mostly isolated fractures. At the end of this stage, five main fault segments have developed (F1 - F5). F1 and F2 are located in the east, whereas F3, F4 and F5 are located to the west in the model.

26.5 – 35.3 % extension

Growth along strike and in slip direction with increasing extension result in linkage of fault segments. F1and F2 link up with adjacent minor faults and grow via sympathetic increase of

length and displacement. These faults overlap and connects the hanging wall with the footwall. Fault F5, which is located to the west in the model, becomes inactive after approximately 29 % extension. The length and displacement of F3 increase with increasing strain. This results in a linkage between F3 and F4, and the development of F3'. F1 links up with neighboring minor faults and fractures. After 35 % extension, three main fault planes have developed across the model (F1, F2 and F3'). Minor fractures have started to develop in the hanging wall. They are mainly located to the left and in the central part of the model.

35.5 - 47.0 % extension

With increasing extension F1, F2 and F3' intersect and link up. This results in a through-going fault, F1' which accommodates most of the displacement at this stage. F1' has an E-W orientation, and shows a curved geometry. The minimum displacement is located in the linkage area between F2 and F3'. As the strain increases, the deformation in the hanging wall to F1' continues. Already established fractures link up, and new fractures develop. The orientation of the fractures in the central part is approximately E-W, whereas the fractures to the west show either an E-W or NW-SE trend.

47 - 73.5% extension

The major fault, F1' becomes inactive after 55 % extension. This means that F1' has been active for 26 % extension. When the major fault becomes inactive, the displacement of minor faults in the hanging wall increases and these accommodate displacement until the end of deformation. Adjacent faults in the hanging wall link up with one another. Some of these faults are connected by relay ramps, and as the extension increases these ramps breach, resulting in linkage of fault segments. At the end of deformation, horst and graben structures are well defined in the hanging wall to F1'. Some areas are more dominated by half grabens, while other areas are dominated by grabens. The orientation of the faults and fractures in the hanging wall is E-W. Some faults show a curved geometry typically located in the linkage area of two faults.

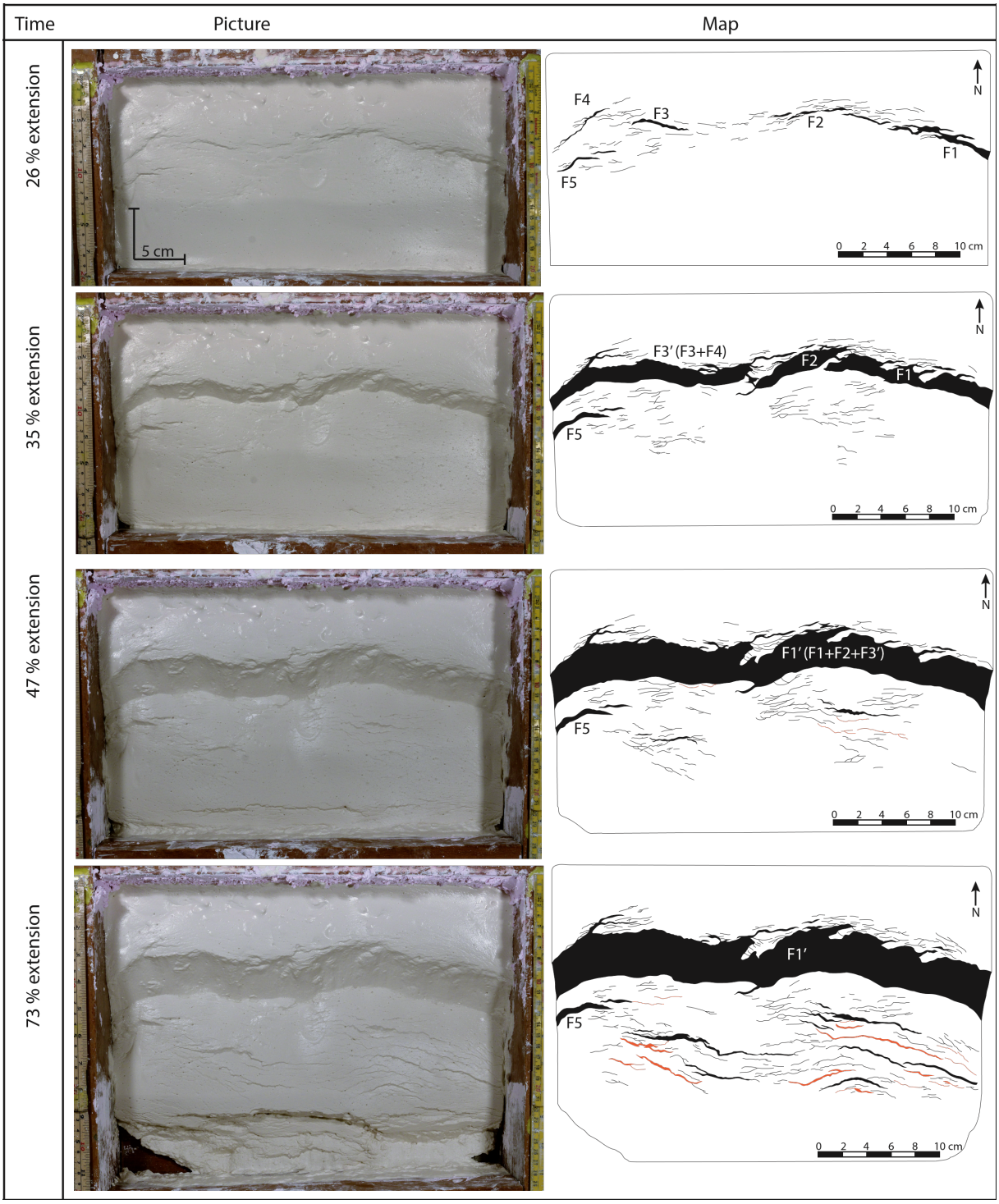

Fig. 5.6: Structural evolution of model 11-15 seen in map view. The black lines and fields represent synthetic fractures and heave. The red lines and fields represent antithetic fractures and heave. Image to the left and line drawings to the right.

Topology of fracture network in model 11-15

The topological analysis of model 11-15 shows the evolution of a fault and fracture network after 35 %, 47 % and 71 % extension. These measurements show that the connectivity is greater in the footwall than in the hanging wall. With increasing strain, more fault and fractures develop in the hanging wall, whereas in the footwall the development and linkage of faults and fractures decrease. The evolution of the connectivity in both the footwall and hanging wall is shown in triangular plots of node and branch proportion. These triangular plots of node and branch proportions show that the changes in the footwall during deformation are smaller than the changes in the hanging wall.

The triangular plot of node proportions (Fig. 5.7a) shows that the proportions of the different node types (I, Y and X-nodes) are close to constant in the footwall. The proportion of I-nodes decreases from 38 % to 36 % during the deformation process. The hanging wall on the other hand, shows an increase. In the early part of deformation, the majority of the faults and fractures appear as isolated segments. The proportion of I-nodes after 35 % extension is 65 % of the total amount of nodes. With increasing extension, the proportion of I-nodes decreases to 55 % in favour of an increase of Y-nodes. The X-node proportion is unchanged during deformation.

The triangular plot of branch proportion (Fig. 5.7b) shows that the average number of connections per branch changes from 1.2 to 1.4 with increasing extension. There is a dominance of I-C branches after 36 % of extension in the hanging wall. As the deformation continues the proportion of C-C branches increases at the expense of I-C branches, whereas the proportion of I-I branches decreases from 10 % to 5 %. In the footwall, the proportion of the different branches is almost constant during the deformation process. The average numer of connections per branch is 1.6 during the deformation of the model.

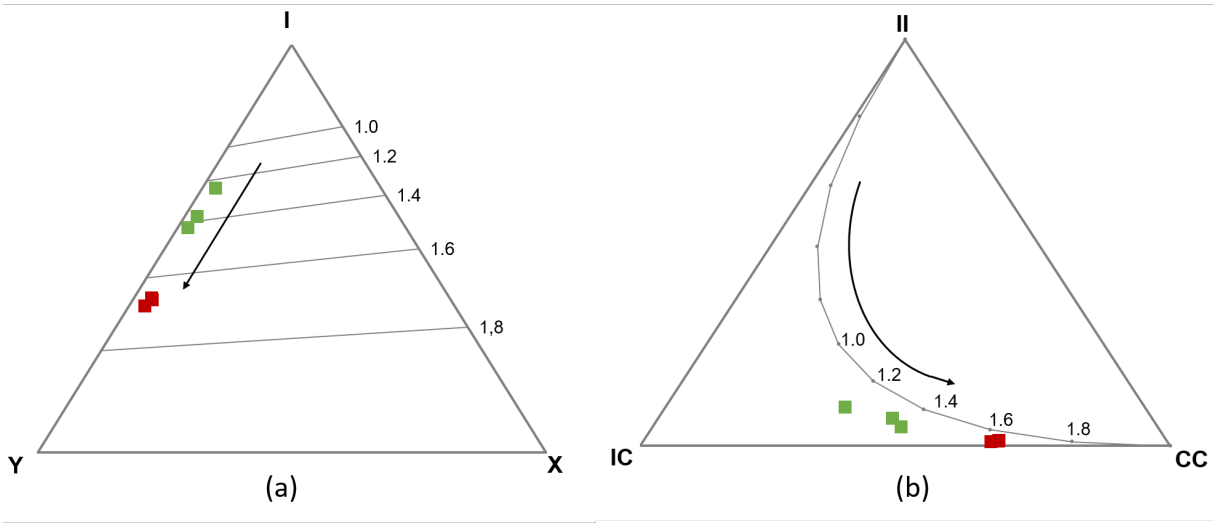

Fig. 5.7: The green and red points are measurements from the hanging wall and footwall, respectively. The arrows show the evolutionary path from a simple network to a more complex one. The numbers 1.0 - 2.0 are numbers of connections per branch (C_B). These measurements are made in the footwall and hanging wall of F1'. (a) Triangular plot of node classification. (b) A triangular plot that shows the proportion of different branch types.

Contour plots of connecting node frequency (Y-nodes and X-nodes) and branch intensity are used to assess the connectivity in a fault and fracture network (Fig. 5.8).

The contour plot of connecting node frequency varies from 0.023 to 0.025 N_C/mm^2 in the footwall as the strain increases. In the hanging wall, the frequency varies from 0.006 to 0.022 N_C/mm^2 during the deformation process. Several bullseyes with connecting nodes can be observed from the plot. These bullseyes are better connected in the footwall than in the hanging wall where they are more scattered. The highest connecting node frequency is located in linkage areas of faults.

The contour plot of branch intensity shows that the intensity varies from 0.14 to 0.19 mm/mm^2 in the footwall and from 0.06 to 0.16 mm/mm^2 in the hanging wall. The contour plot of branch intensity shows that the branches are distributed across the hanging wall and footwall with increasing strain. Some bullseyes with a higher fracture intensity are observed in the model. The majority of these are located in the footwall, although some develop in the hanging wall as the strain increases. By comparing the two contour plots, it is clear that bullseyes with connecting node frequency and branch intensity coincidence.

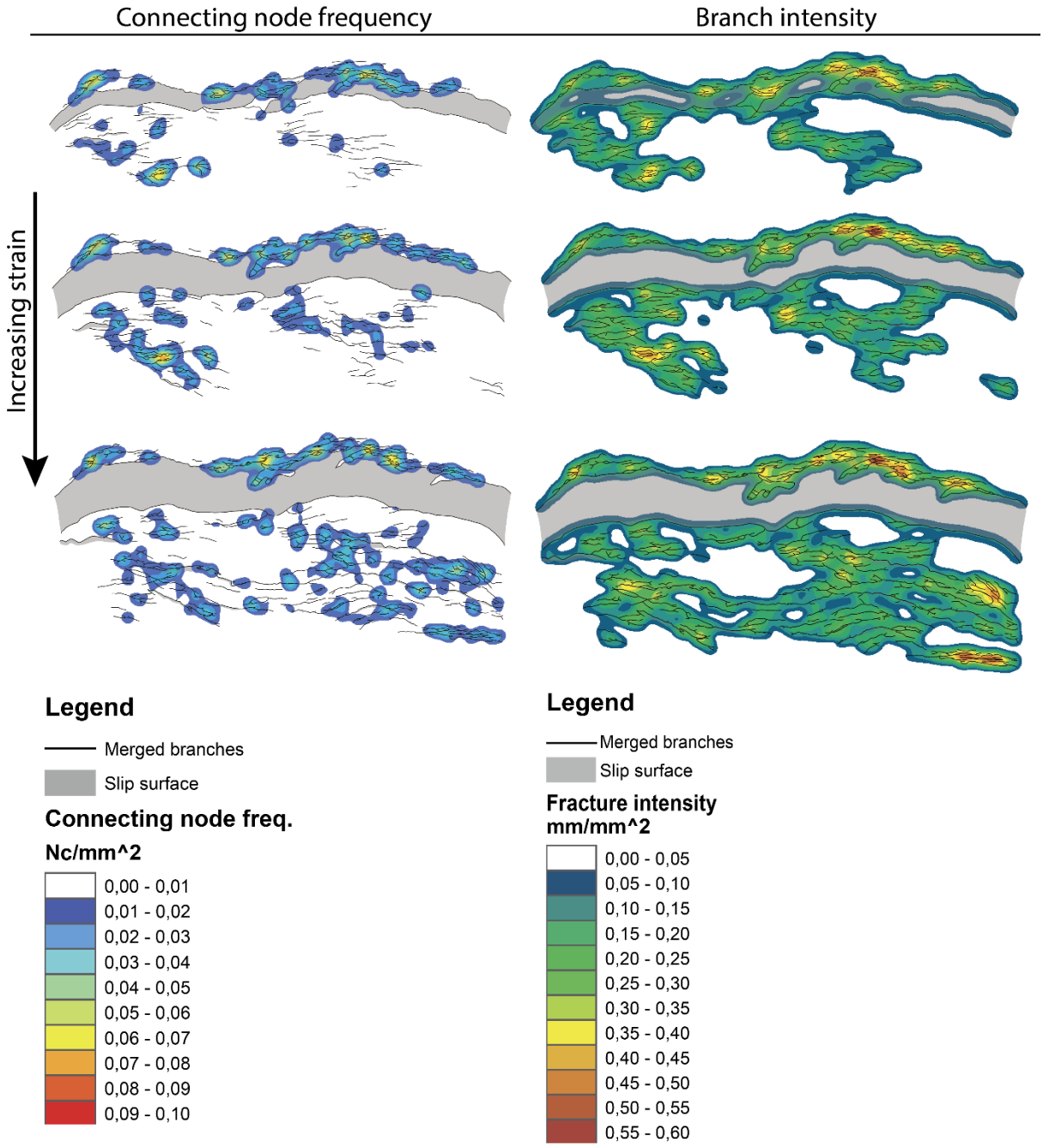

Fig. 5.8: Contour plot of model 11-15 showing the connecting node frequency (left) and branch intensity (right). The three different stages show the evolution of the connectivity with increasing strain. The measurement of the connecting node density is calculated from the number of connecting nodes (N_C) per mm^2, whereas the branch intensity is calculated from the total branch-length (mm) per mm^2.

5.5 Description of experiment 12-15

A stepwise evolution of the deformation throughout the experiment can be followed in figure 5.11. General information about the setup and duration of experiment 12-15 is found in table 5.5. A video of the experiment is found in Appendix A.

Table 5.5: General information about the setup and duration of experiment 12-15

Date	25.11.15
Water plaster ratio	1:1.7
Basal layer	Wedge shaped barite, average slope of ~15^{o}
Initial length	17 cm
Final length	35 cm
Total displacement	18 cm
Total extension	106 %
Duration	39 seconds
Mean extension rate ($\dot{\varepsilon}$)	8.9 mm/s

0 – 26.5 % extension

The first fractures break the surface after ~20 % extension. These fractures are located in the central part of the model and close to the northern corners in the model. The majority of these fractures is orientated E-W, and a minor amount of fractures are orientated NE-SW. These fractures continue to grow as the strain increases. The fractures in the corners grow via sympathetic increase of length and displacement as they link up with adjacent faults and fractures. The fractures in the NE corner intersect with a fault, F1, that is developing adjacent to the back wall. At the end of this stage, F1 overlaps with a fault, F2, that has developed in the NW corner.

26.5 – 29.4 % extension

As the deformation continues, the relay ramp connecting F1 and F2 breaches. This results in the formation of a through-going fault F1', which is located adjacent to the back wall. The orientation of the fault is E-W, and it curves toward the sidewalls. The evolution of minor faults in the hanging wall to F1' continues. An antithetic fault with a curved geometry, F3, has developed in the hanging wall to F1'. In addition, subparallel alignment of separated fractures has developed. They are arranged obliquely to one another, en écholon. F1' accommodates most of the displacement at this stage of the deformation process.

29.4 – 44 % extension

Fault F1' adjacent to the back wall continues to grow and accommodates most of the displacement. Most of the deformation occurs in the hanging wall, where already established faults and fractures continue to grow. Isolated fault segments create several relay ramps across the model as the strike and displacement of faults increases. This results in the development of two main overlapping fault segments (F4 and F5) with an E-W orientation in the hanging wall to F1'. Toward the end of this stage, fractures start to develop south of F5.
The antithetic fault, F2, continue to grow along strike and in slip direction. The increase in strain results in development of new synthetic and antithetic faults and fractures north of F3.

44 – 73.5% extension:

F1' continues to accommodate displacement as the strain increases. The antithetic fault, F3, in the hanging wall to the main fault becomes inactive after 65 % extension. Fractures start to develop in the hanging wall to F1', north of F4 and F5. The length of these fractures are rapidly established and they do only accommodate a small amount of displacement until the breaching of the relay ramp between F4 and F5. The linkage of F4 and F5 results in an irregular fault plane which contains lenses. In the western part of the model in the hanging wall to F4 and F5, fractures start to develop close to the fault with increasing extension. A major antithetic fault, F6, has developed in addition to synthetic faults. Already established fractures start to accumulate displacement in the eastern part of the model. This results in the development of F7.

73.5 – 91.2 % extension:

Fault F1' becomes inactive after 82 %, which means that F1' has been active during 55 % extension. With increasing extension, F4 and F5 link up, creating one fault with an irregular fault plane. In the eastern part of the model, F8 links up with adjacent minor faults and propagates westwards. F4 and F7 overlap after 82 % of extension and develops a relay ramp which breaches after 88 % of extension. The hard linkage of F4 and F7 occur as a mid-ramp breach. The bounded fault segment appears as small splay faults in both the hanging wall and footwall. The breaching of the relay ramp results in a new through-going fault with an E-W orientation in the hanging wall to F1'. Most of the displacement after 82 % extension is accumulated in the hanging wall to the new through-going fault, F4'. These faults and fractures start to develop in the eastern-central part of the hanging wall and in the western

part. They develop as isolated segments, and some of them start to interact and link up at the end of this stage. In the east and west, the fractures are orientated E-W. In the central part, the faults and fractures show a more NE-SW trend in orientation.

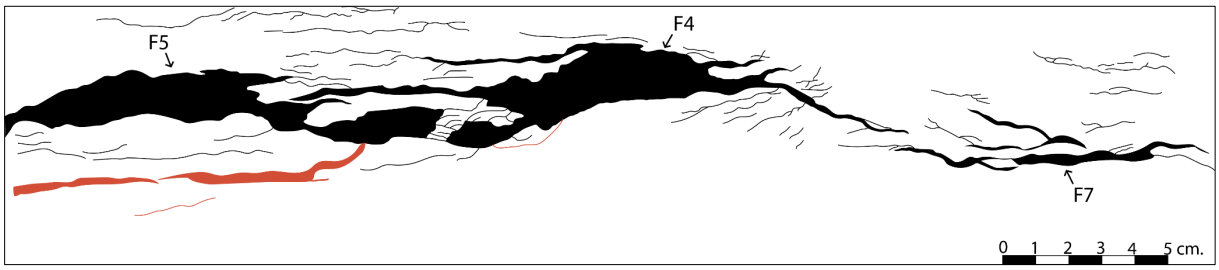

Fig. 5.9: An illustration of the deformation after 79 % of extension showing the linkage of three different fault segments. The black and red lines represent synthetic and antithetic fractures, respectively. The black and red areas represent synthetic and antithetic heave, respectively.

91.2 – 106 % extension:

When the displacement accumulation of F4' decreases, a splaying fault develops in the middle part of the fault. F4' becomes inactive after 100 % extension. This means that F4' has been active for 12 % extension. Overlapping fault segments in the hanging wall to F4' start to link up as the strain increases. This results in the development of a new fault, F8 toward the end of the deformation process. F8 is located in the central part of the model and grows via sympathetic increase of length and displacement as the extension continues. The orientation of the fault varies along strike. The eastern part of F8 is orientated NE-SW, whereas the western part of the fault shows an E-W orientation which is perpendicular to the extension direction. Toward the end of the deformation process, F8 in the middle part of the hanging wall accumulates most of the displacement. Releasing faults form at the fault tip, toward the end of the extension. In addition, some antithetic faults develop in the hanging wall, close to the fault plane of F8.

The fault activity from model 12-15 is summarised in figure 5.10. Fault F3, F4, F5 and F7 develops in the hanging wall to F1' when it still accumulates slip. The linkage of F4, F5 and F7 occur when the main fault has become inactive, and all the displacement is distributed hanging wall structures.

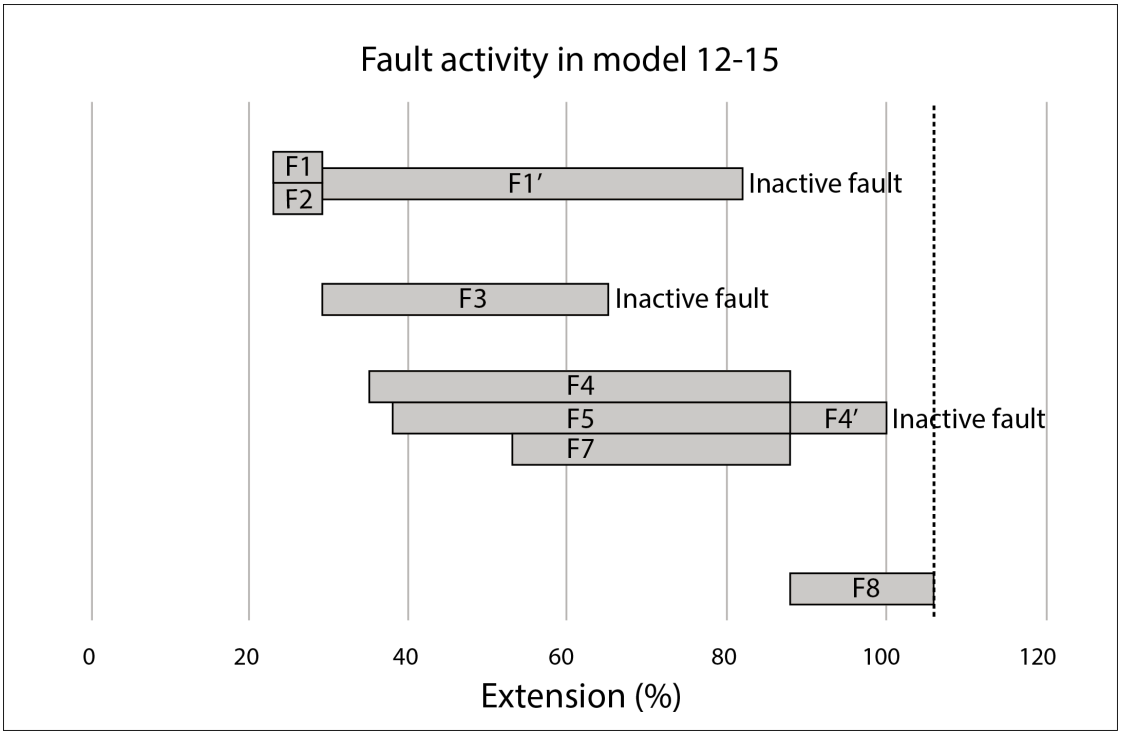

Fig. 5.10: Diagram, which summarizes the evolution and activity of the major faults during the extension in model 12-15. The total extension in this experiment is 106 %, and is indicated by the dashed line. The numbers within the bars indicate the different faults. Faults which link up to develop longer faults are clustered together.

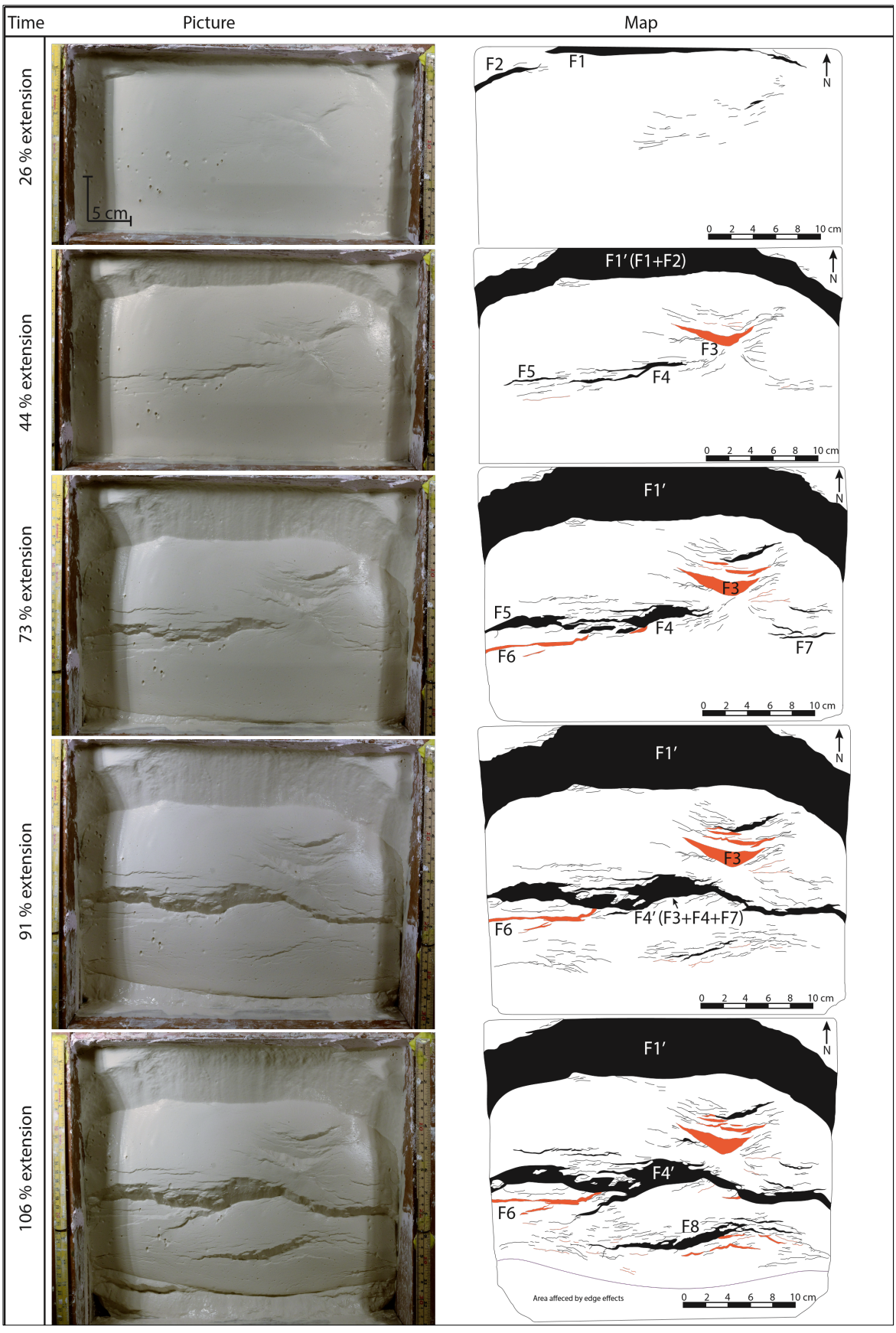

Fig. 5.11: Structural evolution of model 12-15 seen in map view. The black lines and fields represent synthetic fractures and heave. The red lines and fields represent antithetic fractures and heave. Image to the left and line drawings to the right

5.6 Description of experiment 13-15

A stepwise evolution of the deformation throughout the experiment can be followed in figure 5.12. General information about the setup and duration of experiment 13-15 is found in table 5.6. A video of the experiment is found in Appendix A.

Table 5.6: General information about the setup and duration of experiment 13-15

Date:	25.11.15
Water plaster ratio:	1:1.7
Basal layer:	Horizontal barite, 1 cm thick
Initial length:	16.5 cm
Final length:	28.5 cm
Total displacement	12 cm
Total extension	73 %
Duration:	25 seconds
Mean extension rate ($\dot{\varepsilon}$)	11.4 mm/s

0 – 20 % extension

The first fractures break the surface after ~15% extension. These fractures appear as isolated segments and start to curve toward each other with increasing extension, creating longer amalgamating faults. After 18 % extension, F1 has developed to the east in the model. In the central part and toward the west, areas with a high density of fractures are located. With increasing extension, several faults develop along this fractured zone. These faults link up, and after 21 % of extension, two main fault planes, F1 and F2, have developed. Both F1 and F2 grow by intersecting with adjacent faults as displacement is accommodated. They are orientated E-W, and curve toward the sidewalls at the edges. They are overlapping and connected by a relay ramp. Most of the fractures after the formation of F1 and F2 are located in the footwall block.

20 – 32 % extension

With increasing strain, fractures start developing across the relay ramp, which results in breaching of the relay ramp. A through-going fault plane, F1', across the model has developed after 23 % extension. The fault has a curved geometry and an E-W orientation. Most of the displacement is accommodated by F1' at this stage. The deformation in the hanging wall to F1' is located along the fault plane and in front of the fault to the west. These minor synthetic

fractures have the same orientation as the major fault. After the formation of F1', all the traceable deformation is located in the hanging wall to the main fault.

32 – 57 % extension

The major fault F1' accommodates most of the displacement at this stage. The deformation is focused in the hanging wall to F1', where both synthetic and antithetic faults and fractures start to develop. The majority of the antithetic faults are located close to the internal moveable wall. Accommodation zones between synthetic and antithetic faults can be observed in the western part of the model. The orientation of the majority of the faults and fractures are E-W, whereas some rather show a slightly more NW-SE trend. The central part and the right side of the hanging wall only show signs of some small fractures after 57 % extension.

57 – 73 % extension

The major fault accommodates less displacement as the intensity of faults and fractures in the hanging wall increases. The accommodation of slip along strike of the fault is not the same. F1' becomes inactive in the western part of the model after 63 % extension. The east side of the model is active until the end of the deformation process. This means that the major fault accommodates circa 30 % of the total displacement. With increasing deformation, synthetic and antithetic faults start to develop in the central part and to the right in the model. These faults and fractures are orientated E-W. Overall, the majority of the hanging wall deformation is located to the west and the southern part of the model.

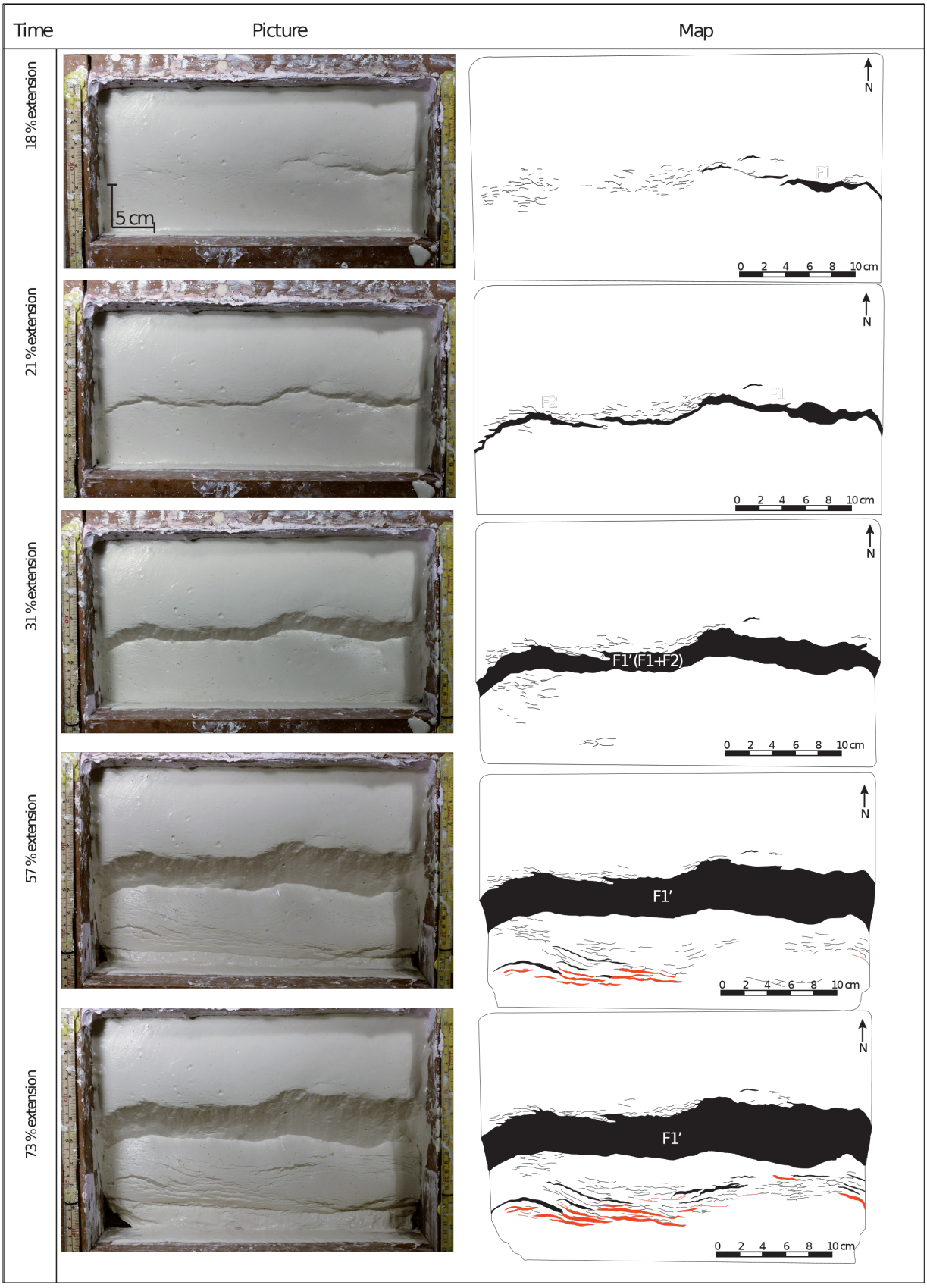

Fig. 5.12: Structural evolution of model 13-15 seen in map view. The black lines and fields represent synthetic fractures and heave. The red lines and fields represent antithetic fractures and heave. Image to the left and line drawings to the right.

Topology of fracture network in model 13-15

The topological analysis of model 13-15 shows the evolution of a fault and fracture network after 21 %, 30 % and 72 % of the total extension. These measurements do not share the same characteristics as the previous models. The connectivity in the footwall is greater than in the hanging wall early in the deformation history. With increasing strain, more faults and fractures develop in the hanging wall. The proportion of nodes and branches in the footwall are more or less constant during deformation while the changes in the hanging wall are bigger.

The triangular plot of node proportions (Fig. 5.13a) shows that the proportion of I-nodes in the footwall only shows small variations (58 to 55 %) during deformation. A small decrease in I-nodes results in a small increase of Y-nodes. The proportion of X-nodes is the same during deformation. In the hanging wall, the proportion of I-nodes decreases from 75 % in the early part of the deformation process to 50 % at the end of the deformation history. The decrease in I-nodes results in an increase of Y-nodes in the fracture network while the X-node proportion is more or less constant during deformation.

The triangular plot of branch proportions (Fig. 5.13b) shows that the average number of connections per branch in the footwall is constant as it is 1.4 during the whole deformation history. The proportion of I-nodes decreases from 11 - 3 %, whereas the proportion of I-C branches and C-C branches is almost constant. There is only small variation of the branch proportions with increasing extension. In the hanging wall, the plotted points are more scattered in the triangular plot. The average number of connections per branch varies from 1.0 in the early part of deformation to 1.5 at the final stage. The proportion of I-I branches decreases from 23 to 5 % in the end. Between stage 2 and 3, the proportion of C-C branches increases at the expense of I-C branches. This shows that the connectivity is better in the hanging wall than the footwall toward the end of the deformation.

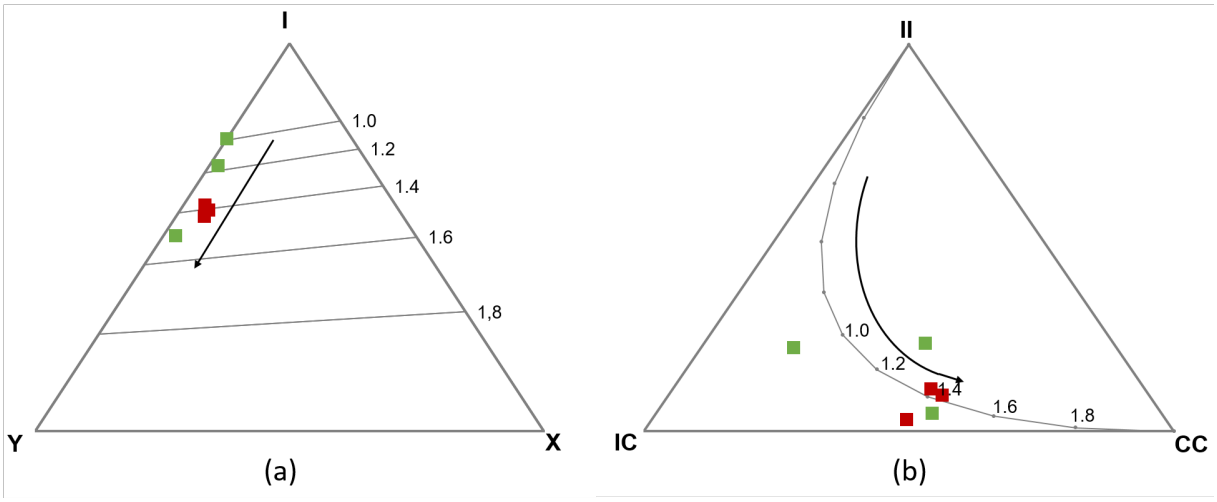

Fig. 5.13: The green and red points are measurements from the hanging wall and footwall, respectively. The arrows show the evolutionary path from a simple network to a more complex one. The numbers 1.0 - 2.0 are numbers of connections per branch (C_B). These measurements are made in the footwall and hanging wall of F1'. (a) Triangular plot of node classification. (b) A triangular plot that shows the proportion of different branch types.

Contour plots of connecting node frequency (Y-nodes and X-nodes) and branch intensity are used to assess the connectivity in a fault and fracture network (Fig. 5.14).

Contour plots of connecting node frequency (N_C/mm^2) show that the frequency varies from 0.007 to 0.011 N_C/mm^2 in the footwall, whereas in the hanging wall it varies from 0.003 to 0.018 N_C/mm^2. In the footwall, the bullseyes with connecting nodes are somewhat clustered, whereas in the hanging wall, they are almost absent. As the strain increases, bullseyes with connecting nodes develop in the hanging wall. These clusters of bullseyes in the hanging wall are connected, indicating a better connectivity.

Contour plots of branch intensity (mm/mm^2) show that the intensity varies from 0.07 to 0.08 mm/mm^2 in the footwall, whereas in the hanging wall it changes from 0.04 to 0.19 mm/mm^2. Bullseyes with a higher fracture intensity are located in the linkage area between two faults in the footwall in the early part of the extension. As the deformation continues, a higher branch intensity is observed in the hanging wall. The bullseyes of connecting nodes and branch intensity coincidence, indicating a better connectivity.

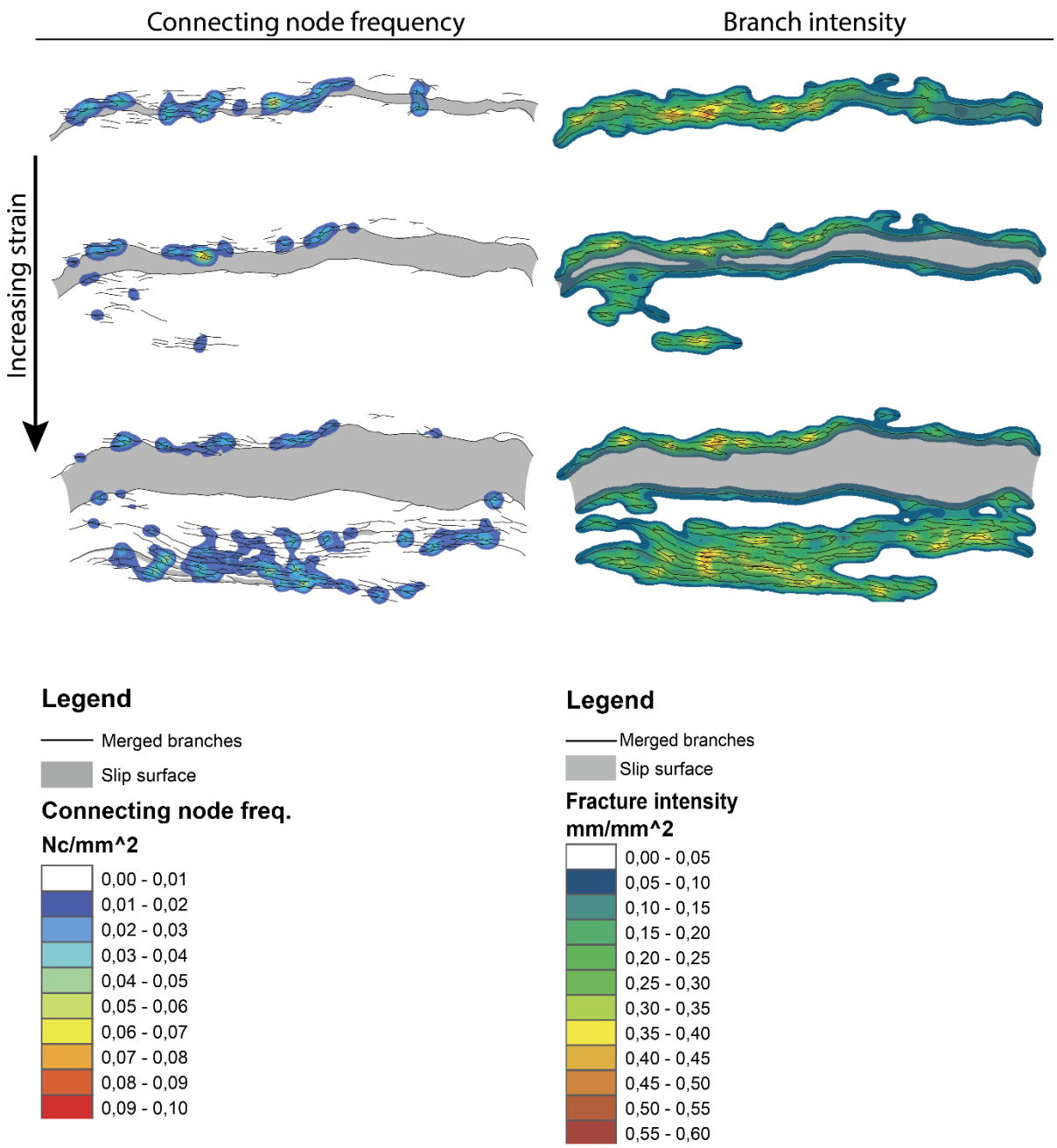

Fig. 5.14: Contour plot of model 11-15 showing the connecting node frequency (left) and branch intensity (right). The three different stages show the evolution of the connectivity with increasing strain. The measurement of the connecting node density is calculated from the number of connecting nodes (N_C) per area (mm^2), whereas the branch intensity is calculated from the total branch-length (mm) per area (mm^2).

5.7 Description of experiment 19-15

A stepwise evolution of the deformation throughout the experiment can be followed in figure 5.16. General information about the setup and duration of experiment 19-15 is found in table 5.7. A video of the experiment is found in Appendix A.

Table 5.7: General information about the setup and duration of experiment 19-15

Date:	10.12.2015
Water plaster ratio:	1:1.7
Basal layer:	Wedge formed barite with an average slope of ~15^{o}
Initial length:	15 cm
Final length:	29 cm
Total displacement	14 cm
Total extension	93 %
Duration	30 seconds
Mean extension rate ($\dot{\varepsilon}$)	9.6 mm/s

0 - 23% extension

Fractures start developing after ~17 % extension. They appear to the north in the model close to the back wall as isolated segments. As the strain increases, these fractures become more defined, and minor faults, F1 and F2, develop. These faults grow via sympathetic increase of length and displacement, and are orientated E-W. F2 is located adjacent to the sidewall in the west and has a curved geometry toward the wall. F1 is located in the central part of the model, and several adjacent minor fault segments have developed. F1 and F2 start to propagate toward one another at the end of this stage.

23 – 30% extension

As the deformation continues, F1 and F2 link up with small fault segments, which already had developed after 23 % extension. This results in the formation of two main fault planes, which grow via sympathetic increase of length and displacement. F1 and F2 propagate toward one another and eventually connect. This leads to the development of a through-going fault, F1', across the model. After the development of F1', most of the deformation is located in the footwall to the fault. Toward the end of this stage, some fractures start developing in the hanging wall to F1'. These fractures are located close to the fault plane and in one area in the

eastern part of the model. the fractures in the hanging wall shows the same E-W trend, although a minor part of the fractures are orientated NW-SE

30 – 43% extension

The small fractures in the hanging wall continue to grow along strike as they accommodate displacement. They are all located to the east in the model at this stage, and start propagating toward the centre and the opposite wall with increasing strain. Some of the fractures in this area develop into antithetic fractures. At the end of this stage, three main fault segments, F3, F4 and F5 have developed. F3 and F4 are overlapping fault segments and are connected by a relay ramp. At the fault tip to the west of F3, fractures intersect the fault with an angle of 45^{o}. The hanging wall fractures are orientated approximately E-W. To the west in the model, fractures starts to develop at the end of this stage. These fractures have a slightly NW-SE orientation.

43 – 56% extension

As the stain increases, F4 and F5 located in the hanging wall to F1' continue to grow along strike as displacement is accommodated and eventually link up. Fractures develop across the relay ramp connecting F3 and F4, resulting in breaching of the ramp as the extension increases, and forms F3'. The displacement changes from being at a maximum close to the centre of each fault segment to having two maximum displacements, one at each side of the breached relay ramp. In addition, a minimum displacement is located where the relay ramp is breached. The fault tip of F3' in the west links up with minor faults and fractures as the displacement and strain increases. To the west in the hanging wall, large fractures evolve and become long defined faults. The fractures link up by curving toward one another. Some of the minor faults have a typically curved symmetry. The dominate orientation of the fractures in the western part of the model is E-W.

56 – 93% extension

The major fault, which developed in the early stage of deformation (F1), becomes inactive after 60 % extension. This means that F1 has been active over 24 % extension.

F3' propagates toward the west in the model, and the faults located in the western part (F6 and F7) propagate toward the east. F6 links up with a fault segment ahead of the fault tip to the east. Once the faults are linked, the final length of the fault is established, and only minor fault tip propagation occurs as the displacement is accommodated. The propagation of the faults results in a new relay ramp between F3' and F6 located almost in the centre of the

model. With increasing strain, the western part of F3' becomes inactive, whereas the eastern part of F3' continues to accommodate displacement until the end of the deformation process. This results in a maximum displacement located to the east in F3'. The hanging wall deformation to F3' occurs toward the end of the total extension. It is mostly fractured, but some minor synthetic and antithetic faults also develop.

A relay ramp develops between fault segments F6 and F7 once they are established. F7 is cut by a fracture with an orientation almost perpendicular to the relay ramp. At the end of the deformation process, the relay ramp is almost double breached.

The fault activity from model 19-15 is summarised in figure 5.15. Fault in the hanging wall to F1' starts developing when the main fault is still active. The linkage between F3, F4 and F5 occur when the main fault is less active, and most of the displacement is accommodated in hanging wall structures in addition to F6 and F7.

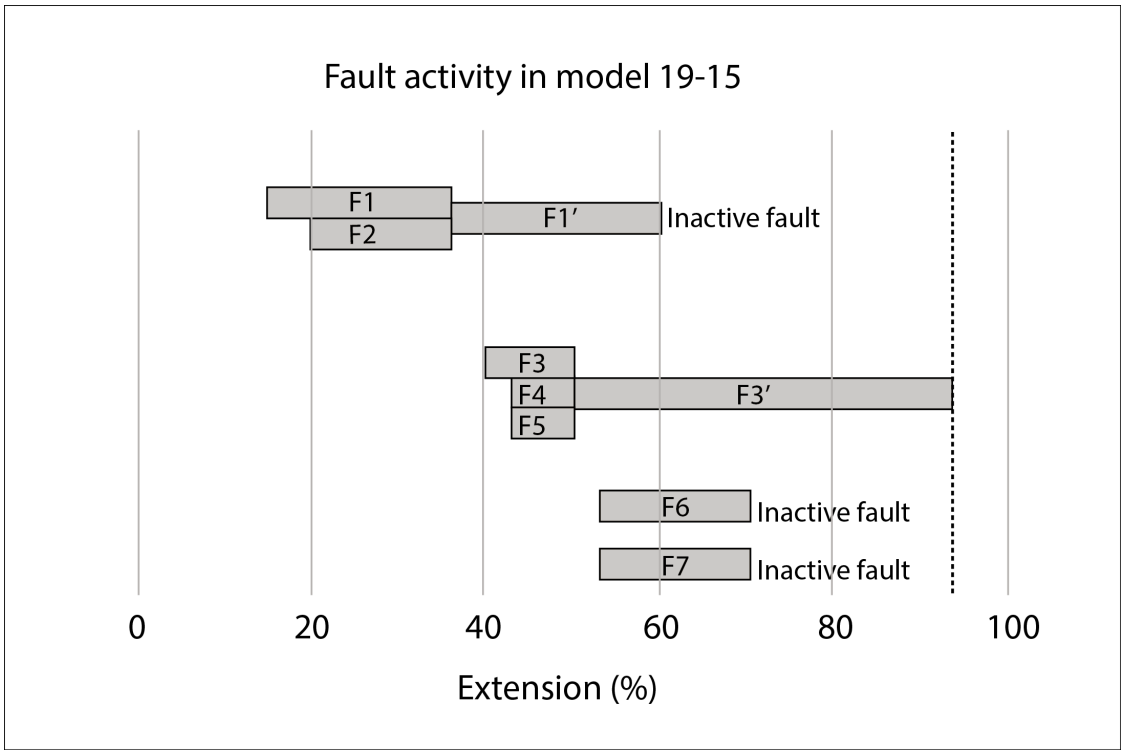

Fig. 5.15: Diagram, which summarizes the evolution and activity of the major faults during the extension in model 19-15. The total extension in this experiment is 93 %, and is indicated with a dashed line. The numbers within the bars indicate the different faults. Both F3', F6 and F7 are located in the hanging wall to F1', which is the reason why they all are active at the same time in the model. Faults which link up are clustered together.

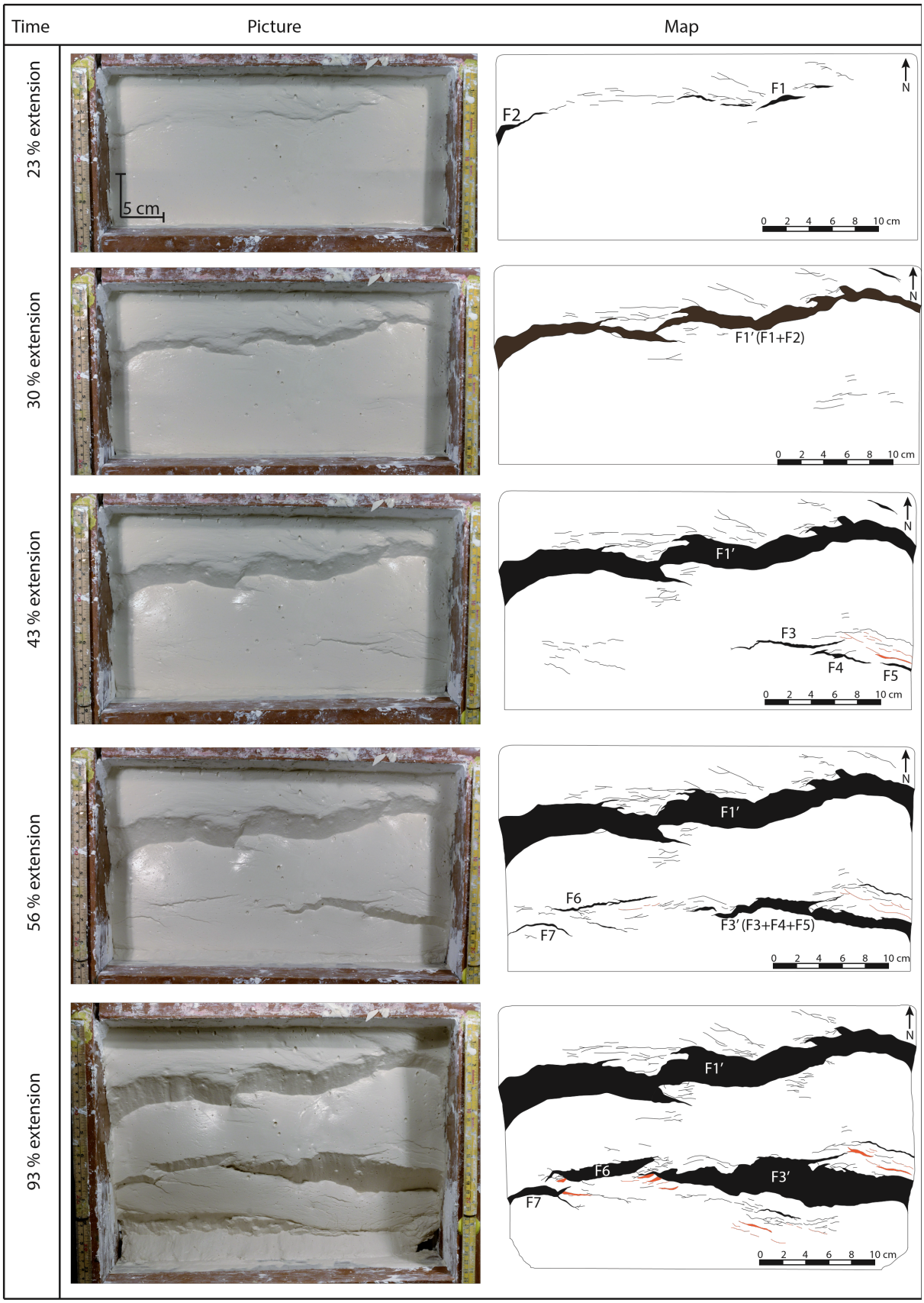

Fig. 5.16: Structural evolution of model 19-15 seen in map view. The black lines and fields represent synthetic fractures and heave. The red lines and fields represent antithetic fractures and heave. Image to the left and line drawings to the right.

5.8 Displacement with fault length

Displacement accumulates along the faults during deformation of each experiment. The maximum displacement is plotted against the fault length of different faults in the models, both major and minor faults. These plots illustrate the change in maximum displacement as the fault length increases.

The displacement length-time plot illustrates the different evolution patterns of faults found in analogue models (Fig. 5.17). Some faults grow via sympathetic increases of displacement and length (fault 1, 5, 7 and 12). Fault 1, 5 and 7 are a result of linkage between fault segments, whereas fault 12 grows as an isolated fault. The buckling point in the curve occurs when two faults link up. This results in a rapid increase of the fault length when two segments interact. After the fault segment linkage, the displacement increases more than the length of the different faults.

Other faults show a rapid establishment of the final fault length and subsequent displacement increase with minor tip propagation (fault 2, 4, 9,10, 11, 13 and 14). Fault 3, 6 and 8 show a two-step model where the length accumulation dominates until the maximum length is achieved. When the maximum length is achieved, the fault accommodates displacement along the slip surface and only minor tip propagation along the strike of the fault occurs.

A total of 44 measurements have been used to illustrate that there is a positive correlation between maximum displacement and length of the faults (Fig. 5.18).

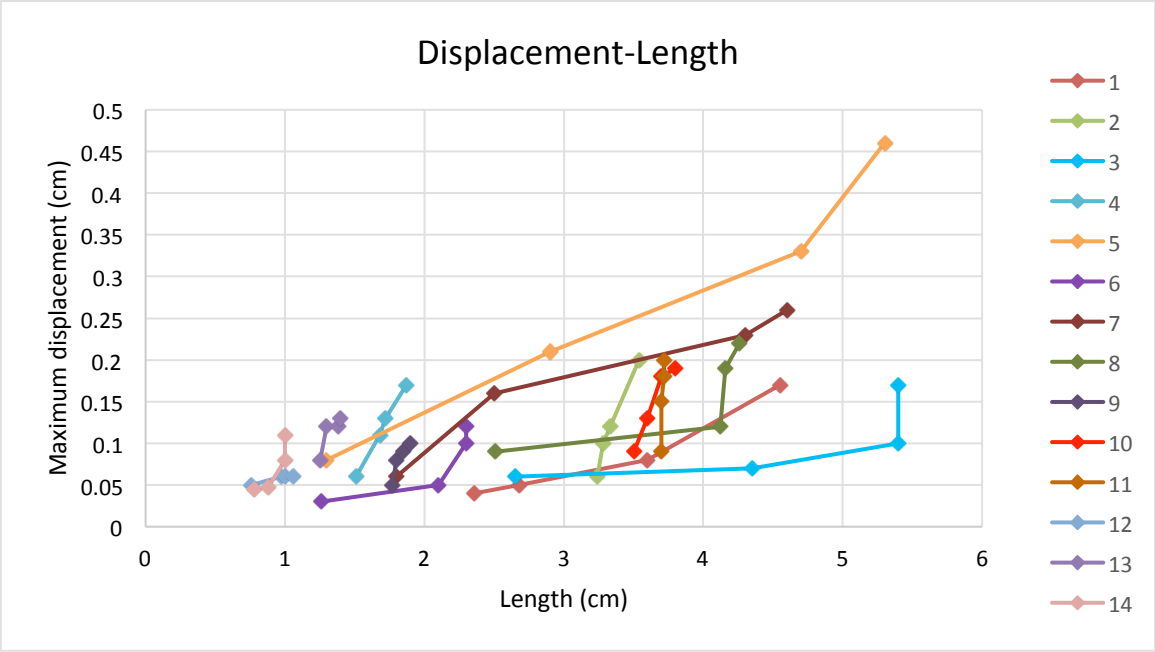

Fig. 5.17: Illustration of the relation between length and displacement of 14 different measured faults. These measurements show that fault growth is not constant, but there is a positive correlation between length and displacement. The time relation between fault length and fault displacement is not to scale.

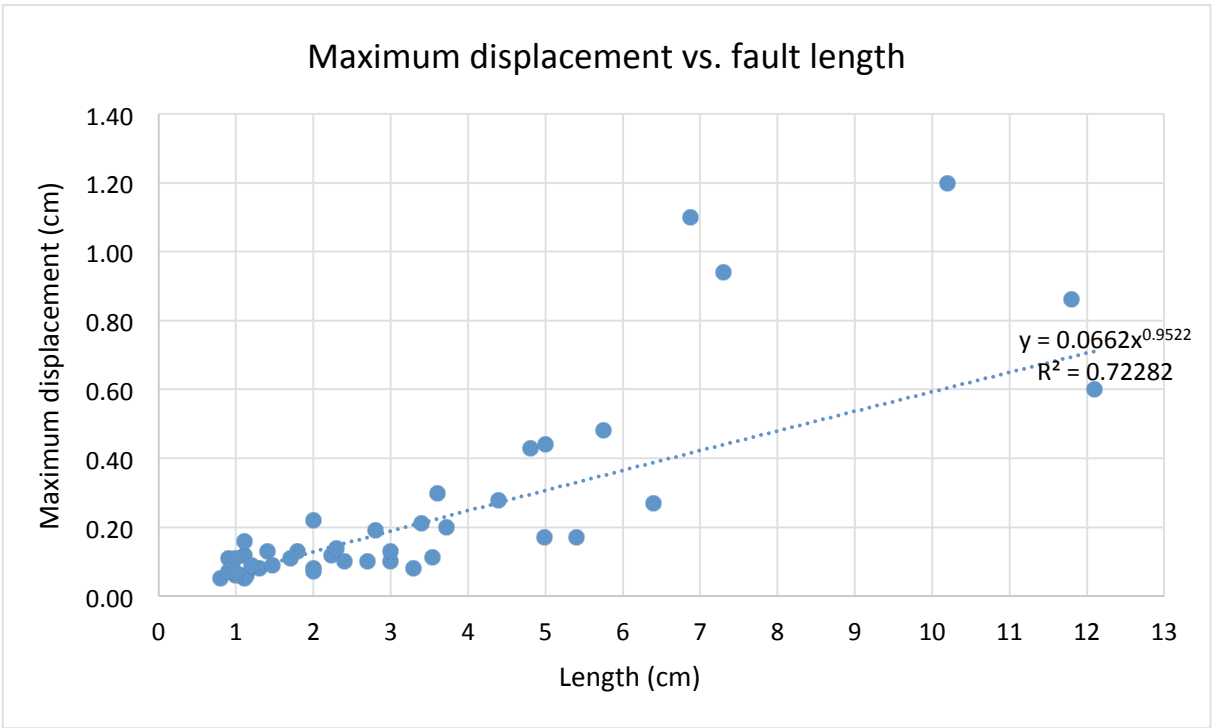

Fig. 5.18: Correlation between fault length and maximum displacement of the fault.

5.9 Summary

5.9.1 Analogue models

Two different basement shapes have been used in the experiments, wedge-shaped and horizontal barite. The basement shape influences the fault geometry in each model. A horizontal basement results in one main fault across the model. The majority of minor faults and fractures develop in the hanging wall to the major fault when the main fault accommodates less displacement and is close to dying out. These secondary structures accommodate most of the displacement when the major fault has become inactive.

Models with a wedge-shaped basement develop several fault planes across the model. The first fault develops close to the back wall/northern wall. The second through-going fault develops later in the experiment and accumulates most of its displacement when the first fault becomes inactive. In general, despite the shape of the basal layer, a through-going fault plane develops across the model at ca. 29-35 % extension. The main through-going fault accommodates most of the displacement in all of the models.

5.9.2 Topology

The topological analysis of model 5-15, 11-15 and 13-15 shows that the connectivity is greater in the footwall than in the hanging wall in the early stage of deformation (20-30 % of extension) in all analysed models. With increasing extension, the topology in the hanging wall becomes more complex, while the plotted points from the footwall are more clustered and only show small changes. Toward the end of deformation, the connectivity is more or less the same in both the footwall and the hanging wall.

The triangular plots of node proportions show the evolution of the connectivity from all models in both the footwall and hanging wall (Fig. 5.19a). In general, this shows that the connectivity in the hanging wall is lower than in the footwall, and the variation is greater in the hanging wall.

The triangular plot of branch proportions shows that the plots from the footwall are more clustered than for the hanging wall (Fig. 5.19b). In addition, the proportion of C-C branches is in general higher in the footwall than in the hanging wall.

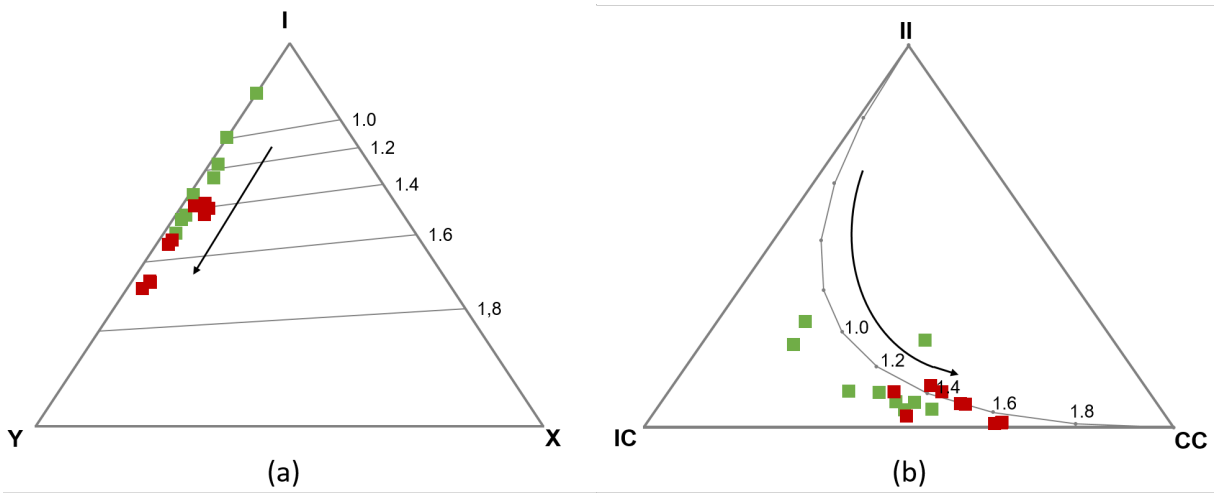

Fig. 5.19: The green points represent data from the hanging wall and the red points represent data from the footwall. The arrow indicates that the fault and fracture network goes from simple to a more complex network. The number 1.0 - 2.0 are connections per branch (C_B). (a) A triangular plot of node proportions from all the investigated models. (b) A triangular plot of branch proportions.

5.9.3 Displacement-length

Faults in the displacement/ length-plot show that the fault growth in analogue plaster models are not consistent. Some faults grow by an increase of both the length and heave as the extension increases, whereas other faults have a rapid establishment of their length and only show minor tip propagation as the fault accommodates displacement. There is a positive correlation between fault length and the maximum displacement of the faults.

CHAPTER 6 – DISCUSSION

6.1 Introduction

The main aims of this thesis have been to gain insight into fault growth, damage zone evolution and to get a better understanding of how the topology and thus connectivity of a fault system evolves with increasing strain. In this chapter, the results of the study are interpreted and discussed in the light of the aims, placing the results in a bigger context. The results are later compared with other analogue models, numerical models and natural examples.

6.2 The influence of basement geometry

Two different kinds of basement geometry have been used in the presented experiments, a horizontally arranged barite layer (model 5, 7, 11 and 13) and a wedge shaped barite layer (model 12 and 19). The geometry of the presented models reflects the shape of the basement (Fig. 6.1). The results show that the basement geometry strongly affects the hanging wall deformation in analogue models. In the cases where the basement is a horizontal layer of barite, only one main fault plane develops, and the deformation is mostly located in the hanging wall to the main fault (Fig. 6.1a). The hanging wall deformation occurs toward the end of the deformation process when the main fault accommodates less displacement and eventually becomes inactive. A wedge shaped basement (Fig. 6.1b) results in two main faults cutting across the models. One fault is located adjacent to the northern wall, situated at the upper edge of the wedge, whereas the other one develops in the hanging wall as the strain increases. The second main fault in the models has a more irregular fault surface and is less developed, as several minimum displacements can be observed along the strike in addition to nearly breached/breached relay ramps.

The different fault geometries which develop in the models with a different basement can be explained by the distribution of forces. The shear forces acting in models with a wedge-shaped basement are greater than in the models with horizontal barite due to the angle of the slope. In the models with wedge shaped barite, shear stresses occur even without extension, since an initial shear stress is induced by the gravitational force on the tilted plane.

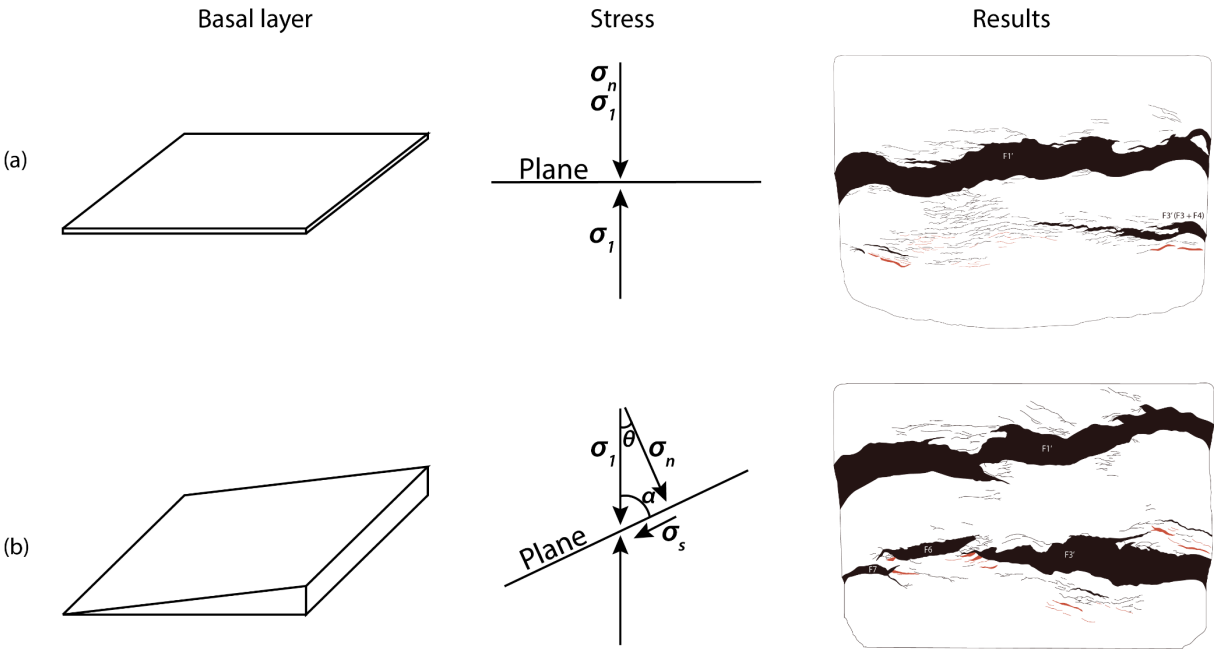

Fig. 6.1: (a) By using a horizontal basal layer, one fault accommodates most of the displacement, whereas the rest is distributed in several minor faults. The stress acting prior to faulting is normal stress. (b) By using a wedge shape basal layer, the displacement is restricted to less, but more developed structures. The stress acting prior to faulting is both shear stress and normal stress.

6.3 Fault growth and linkage

Two models of normal fault growth have been accepted. One model is known as the *"isolated fault model"* or *"fault growth by segment linkage"* where faults grow and eventually linkage of isolated fault segments occurs (e.g. Cowie and Scholz (1992c), Cartwright et al. (1995), Rykkelid and Fossen (2002)). The other fault growth model suggests that isolated faults at the surface are mechanically linked in the subsurface. This model is known as the *"coherent fault model"* (Walsh et al., 2002, Walsh et al., 2003).

6.3.1 Fault initiation

The analysed models show the first sign of brittle deformation between 13 - 20 % extension (average 16 %). This is later than in other analyses, e.g. Bøyum (2015), which found that the first fractures were initiated between 2 - 10 % extension. This later appearance of faults at the surface is a result of fault initiation and propagation from the centre of the fault, resulting in folding at the surface prior to faulting (Grasemann et al., 2005).

The plaster-water ratio is the same for all the experiments presented in this thesis, but the viscosity of the plaster is not constant in each experiment since it changes with time. With a simple method like the one used for this thesis, it is not possible to have the same plaster

viscosity in all models. However, the viscosity variation in the models selected for further analysis is probably quite small, as the majority of the structures resemble structures found in nature. If the plaster was too stiff when the experiment was initiated, the slip would be restricted to only one major fault. If the plaster was too soft, ductile deformation would dominate the model.

6.3.2 Fault interaction and linkage

Linkage of fault segments is an important mechanism for fault growth (Peacock and Sanderson, 1991, Cartwright et al., 1995, Nixon et al., 2014).

Interaction between isolated fault segments is likely to occur as the faults grow. The interaction between adjacent faults can be divided into four different main types suggested by Fossen et al. (2005). These types being; crosscutting, mutual interaction, single tip interaction and double-tip interaction. Crosscutting and mutual interaction will not be preserved in the analogue plaster models as they are constantly developing. Another important factor for developing crosscutting and mutual interaction are faults and fractures that develop with an oblique angle to one another (Duffy et al., 2015) . Crosscutting and mutual interaction are therefore more common where two generations of faults develop, often with an oblique angle to each other. In this thesis, only one generation of faults is developed, and the analysis of analogue plaster models has shown that single tip interaction between faults is most common. This is also what we would expect in a single extension phase. Double-tip interaction has also been observed, although it is not common in the plaster models.

From the analysis of analogue models presented in the results, single tip breaching of relay ramps seems to be most common, although occasionally, mid-ramp breaching and double tip breaching occur. The linkage between F3' and F7 in model 12-15 is a good example of mid-ramp breaching. The different breaching geometries are most likely affected by the viscosity of the plaster when the relay ramp breaches. The breaching of the relay ramp between F3' and F7 occurs after 88 % extension. This suggests that mid-ramp breaching is more favourable in deformation of more brittle nature since the viscosity of the plaster increases with time. Although due to the lack of more data when it comes to mid-ramp breaching this cannot be further discussed. However, Fossen and Rotevatn (2016) have also suggested that mid-ramp breaching is favourable in more brittle rocks.

Numerical models of relay ramps from Crider and Pollard (1998) suggest that the breaching of relay ramps is expected to occur in the middle to upper part of the ramp where the stress is

greatest. A numerical model by Imber et al. (2004) and analogue sand experiments by Hus et al. (2005) found that there were no consistence in where breaching occurred as both upper and lower breaching of ramps developed, although lower ramp breaching/hanging wall propagation was slightly more common. This is not consistent with the result from the plaster models. Firstly, a measurement of 14 relay ramps was done, where eight of them were breached in the middle to upper part of the relay ramp and the remaining six were breached in the lower part of the relay ramp. These results do not show any clear signs that the breaching should occur in the middle to the upper part as suggested by Crider and Pollard (1998). Secondly, there was no consistency in when the breaching of the different relay ramps occurred in the model, except the breaching in the middle of the ramp which occurs late in the deformation process when the plaster is more viscous. Although as mentioned earlier, lack of data cannot confirm this. The result suggests that the location of breaching is not consistent, as both upper and lower breach seem to be common from the analogue models. In contrast, according to Hus et al. (2005) data from natural examples shows that footwall breaching is more commonly observed.

6.3.3 Displacement - length relationship

The relationship between fault displacement and fault length is analysed during studies of faults. The faults chosen for analysis of displacement-length ratio (fig. 5.17) are those which do not interact with the walls (have free tips). This explains the relatively small number of faults used in the plot as no major faults could be used. A wider model may account for this, resulting in a greater number of faults with free tips. However, by analysing the photos and videos, the major faults are thought to grow and propagate as the displacement is accumulated, following the “isolated fault model”. From figure 5.17 it is concluded that there is not a constant relationship between fault length and displacement. Instead, the relationship evolves as the fault population grows.

From the displacement length-plot is it clear not all faults from analogue plaster models follow the same growth trajectory in x-y direction. The displacement-length plot of fault number 2, 4, 9, 10, 11 ,13 and 14 from the plaster models display a nearly vertical trajectory, where the near-final fault length is rapidly established, and only minor further fault tip propagation occurs as more displacement is accrued. This is consistent with the alternative fault growth model suggested by Walsh et al. (2002). It is suggested that the “coherent fault model” is best suited for reactivated fault systems with vertical or lateral splaying from a single fault (Walsh et al., 2003, Jackson and Rotevatn, 2013). However, in this case, the initial

length is not initiated by pre-existing structures as suggested above. This may suggest that the coherent fault model also can be applied to faults which are not initiated by pre-existing structures.

The analysis of faults from analogue models (fig. 5.17) shows that some faults reflects a bimodal growth as they are found to grow in two different phases. One phase is dominated by lengthening whereas the other phase is dominated by accumulation of displacement. This can be observed from fault 3, 6 and 8. According to Schlagenhauf et al. (2008) both of these phases have been observed in nature, although describing them in detail has not been possible due to the long fault lifetime. However, analogue models give the opportunity to study the evolution of fault growth. The analysis of fault growth of fault 6 and 8 from fig. 5.17 shows that the nearly final length of these two faults is rapidly established, approximately after $^1/_3$ of the activity to the fault. The remaining $^2/_3$ of the fault activity are dominated by accumulation of displacement. In the lengthening phase, only minor parts of the displacement are accumulated. Minor tip propagation occurs as the fault accumulates most of the displacement in the second phase. This is consistent with the results from analogue experiments by Mansfield and Cartwright (2001) and Schlagenhauf et al. (2008) which also found that faults grow in two phases; first, there is a short period dominated by rapid lengthening followed by a longer period with subsequent displacement accrual with no or little tip propagation. Fault 3 is a result of linkage of two fault segments. The linkage results in a rapid increase of fault length, approximately after ¼ of the lifetime of the fault. Displacement dominates the remaining ¾ of the fault lifetime. All these faults show that the lengthening activity is shorter than the displacement accumulation. This indicates that there is a delay of accommodation of slip for the different faults. An elastic response of the plaster may explain this behaviour in the models. According to Walsh et al. (2003), a delay in slip accumulation is consistent with the isolated fault model where the displacement accumulation is not continuous.

The plaster viscosity increases with increasing extension and eventually becomes too stiff to deform. Thus, the final results from the models do not necessarily reflect a mature system in nature. In the end of the experiments, some faults could still accumulate slip at a constant length. In nature, it is found that the ratio between slip and fault length reached a threshold (Manighetti et al., 2001), as the slip cannot be accumulated in infinity without lengthening. Fault 8, 9 and 10 from figure 5.17 show a resume of lengthening after the slip has been dominating, suggesting that after a certain ratio between length and displacement is reached,

lengthening is resumed as long as there is no barrier, e.g., arrested fault tips. In such cases, slip may continue to be accumulated. This can also be emphasised by the pot of maximum displacement length which shows a nearly a linear relationship between maximum displacement and length (discussed later in the text).

The analysis of fault growth shows that linkage of two faults results in a rapid increase of fault length while the accommodation of the displacement is delayed. From the displacement-length plot, two buckling points can be identified. In the first one, the linkage of faults occurs, resulting in a sudden increase of fault length. In the second one, the displacement is accommodated rather than the length, resulting in a steeper slope. This is consistent the literature, e.g. Peacock and Sanderson (1991), Cartwright et al. (1995) and Schultz and Fossen (2002) which suggested a step-like growth curve from the model "fault growth by segment linkage". Three of the in total 14 analysed faults (fault number 1, 5 and 7) grow by linkage of fault segments with a sympathetic increase of fault length and displacement.

The wide variety of fault growth from analogue models may suggest that the lithological effect on displacement/length-ratio only plays a minor role compared to other factors such as spatial distribution of faults and their stress fields. This can be explained by the homogenous of the plaster.

6.4 Progressive evolution of connectivity in fault damage zones

The topological analysis and the triangular plots of node and branch proportions are quantitative measurements of the connectivity of the studied fault and fracture network. In addition, contour plots of connecting node frequency and branch intensity are used to assess the spatial distribution of the connectivity in the hanging wall and footwall at different time steps, to understand the evolution of connectivity over time.

6.4.1 Damage zone evolution

It is important to understand the damage zone as it plays an important role for fluid flow evaluation. The origin and evolution of the damage zone in nature are hard to understand as nature only reveals the intensity and spatial distribution in a snapshot of time. However, analogue models can reproduce the evolution of the damage zone in fault systems as the strain increases.

Due to the homogenous plaster the structures and extent of these structures would be expected to be more or less the same at each side of the fault. However, this is not the case. The

damage zone in the footwall is smaller than the damage zone in the hanging wall. Analysis of the analogue plaster models shows that the damage in the footwall does not develop further after the development of the main fault. The damage is initiated prior to the main fault development and the damage intensity decreases away from the main fault in the footwall. Comparable results have been well documented by e.g. Janssen et al. (2001) and Mitchell and Faulkner (2009).

In the beginning, the damage appears as isolated fractures. As the strain increases the fractures start to interact and link up forming locally better connected systems. In the hanging wall it is well illustrated that the damage zone complexity increases with increasing strain. This is consistent with field data from Kim et al. (2003). In the analogue models, splaying structures are common in the damage zone in both footwall and the hanging wall. These splaying structures are in some cases established once the fractures become visible at the surface, indicating that they do not have to be a result of linkage of segments with increasing strain and/or the time-lapse from the cameras do not capture the linkage.

6.4.2 Connectivity in fault and fracture networks

The analysis of fault and fracture networks in model 5-15, 11-15 and 13-15 shows that there is a general trend that the connectivity is better in the footwall than in the hanging wall in the early part of the extension history. This can be seen from the triangular plots of node and branch proportion from the different models (fig. 5.3, fig. 5,7 and fig. 5.13). As the strain increases, the proportion of the different nodes and branches changes. In the footwall, these changes are relatively small compared to the hanging wall. In the hanging wall, the proportion of I-nodes and I-I branches decreases whereas the proportion of Y-nodes and I-C and C-C branches increases. As the strain increases, isolated fractures link up with adjacent fractures. This results in an increase of connectivity. An increase of Y-nodes and I-C branches is characterised by splaying faults, whereas an increase in Y-nodes and C-C branches characterise breaching of relay ramps. The analysis of the models also suggests that once the main fault has developed, the deformation in the footwall more or less ceases, whereas the deformation in the hanging wall increases. This explains why the damage in the footwall remains relatively unchanged compared to the hanging wall which is active until the end of the deformation history. According to Berkowitz et al. (2000), connectivity depends on the fracture size, density and the orientation and spatial distributions of the fractures. From the analysis of the plaster models, it is clear that the connectivity of a fault and fracture network also is highly dependent on topology and strain as fault and fracture networks appear to be

better connected with increased strain. This is well illustrated from the triangular plots of node and branch proportion (fig. 5.3, fig. 5.7 and fig. 5.13) which show that the average connections per branch (C_B) increases with increasing strain. Higher average C_B indicate that more branches must be connected, which then again indicates that the connectivity increases. This is consistent with studies from, e.g. Gupta et al. (1998), Ackermann et al. (2001), Henza et al. (2010) which state that a fault system becomes better linked with increasing strain, ergo, a higher average C_B in the network. This also suggests that the connectivity increases with increasing deformation.

6.4.3 Contour plots

Contour plots of connecting node frequency and branch intensity (fig. 5.4, 5.8 and 5.14) show clearly that there are big variations in damage along the fault plane in addition to the hanging wall and footwall. Bullseyes with more intense deformation are located in the linkage area/interaction area of two faults. This zone with higher damages is consistent with findings from nature e.g. Fossen et al. (2005), De Joussineau and Aydin (2007). Based on the findings from my analogue models it is clear that the highest damage along strike is located in the linkage area of two faults. In these areas, bullseyes with connecting node frequency and branch intensity coincide, which suggests that these areas in the model show more complex faulting and are better connected than the wall damage zone and tip damage zone.

The generally higher connectivity in the footwall of models 5-15, 11-15 and 13-15 than in the hanging wall can be explained by clustering of branches and connecting nodes. In model 5-15, clusters with connecting nodes (fig. 5.4) are widespread along the main fault in the footwall and across the whole hanging wall. After the deformation process, clusters with high node frequency coincide with areas with a high branch intensity. There are mainly two areas with a much higher density of both connected nodes and branches where the connectivity is better than in the surroundings. Although these two areas are not connected, fluids may therefore not be able to percolate between them. In the footwall, only minor clusters with a lower node frequency are located along the fault plane. If we could assume that the fault itself acts as a migration pathway for fluids, all clusters that are connected to the fault plane would be connected. In addition to these clusters, splaying fault with a locally higher node frequency

In model 11-15, clusters with a higher connecting node frequency (fig. 5.8) are often widespread across the hanging wall and appear as bullseyes. This indicates that there are areas in the hanging wall with high connectivity, but since these cluster are not connected, fluids

may not be able to percolate between them. The connectivity in the hanging wall as a whole would therefore be lower than what it appears as when just the fracture intensity is considered. In the footwall, most of the clusters with high connecting node frequency and branch intensity are located along the fault plane. If we could assume that the fault itself acts as a migration pathway for fluids, all clusters connected to the fault plane would be connected. The triangular plots of node and branch proportions (fig. 5.7) also emphasise this.

The isolation of clusters with high connecting node frequency and branch intensity explains why the connectivity is better in the footwall than in the hanging wall in model 5-15 and 11-15. Several isolated clusters of connecting node frequency in the hanging wall suggest a relatively high proportion of I-C branches. This means that faults and fractures in the hanging wall can create several clusters with locally good connectivity, but the ability for fluids to percolate between the different clusters is small. This indicates that the total connectivity is lower in the hanging wall than in the footwall where a majority of the clusters are connected to the main fault plane. However, we do not know how these faults look like in a three-dimensional perspective. As seen from the displacement-length plot, some faults are suggested to follow the coherent fault model suggested by Walsh et al. (2002), Walsh et al. (2003). If this is the case, faults may be mechanically linked in the subsurface, meaning that also the clusters can be connected in the subsurface. The connectivity may therefore be higher than it appears at the surface. In other words, the connectivity measurement from the surface is a minimum estimate.

In model 13-15, clusters with connecting node frequency are located in the footwall along the fault plane, in the footwall after 21 % extension. The areas with the higher frequency coincide with the areas with higher branch intensity. Even though the clusters in the footwall are not connected, the connectivity in the footwall is relatively large compared to the hanging wall as most of clusters are connected to the main fault. The deformation of the hanging wall increases as the strain increases. In this model the deformation results in a connection between the clusters in the hanging wall, resulting in better connectivity than in the footwall.

The results from the plaster models are consistent with the results from Micarelli et al. (2006a) and Micarelli et al. (2006b) which showed that the damage zone has a higher fracture density and thus better connectivity than the surroundings. Their results show that the damage increases and becomes more intense toward the fault plane. This is consistent with literature describing structures in nature, e.g. De Joussineau and Aydin (2007) . However, this can only

be observed in the footwall to the main faults from analogue plaster models. There is no evidence that the damage increases toward the fault plane in the hanging wall.

6.5 Comparison with nature

Analogue models provide a unique opportunity to analyse and quantify the fault growth process, and they exhibit a number of features and geometries of faults observed in nature. Here, parts of different models are compared with field examples.

6.5.1 Relay ramps

The geometry, interaction and linkage in analogue models shows similarities with observations from nature. The evolution and linkage process observed in analogue models cannot be observed in nature, but models of the evolution (e.g. Peacock and Sanderson (1991) and Peacock and Sanderson (1994)) give an insight into the different processes operating. In the analogue models, stage 1, 2 and 4 are common, whereas stage 3 with secondary fracturing across the ramp is only occasionally observed, typical in the largest ramps. In nature, it is well known that secondary structures develop across the relay ramp prior to breaching e.g. shear bands (Kristensen et al., 2013) and deformation bands (Fossen et al., 2007). This may suggest that the plaster itself is too coarse to produce such small fractures in the minor ramps and/or the resolution of the cameras to capture such minor fractures is not high enough. Nevertheless, analysis of plaster models can still give detailed insight into the growth and linkage of faults and show remarkably similar structures as natural examples (Fig. 6.2).

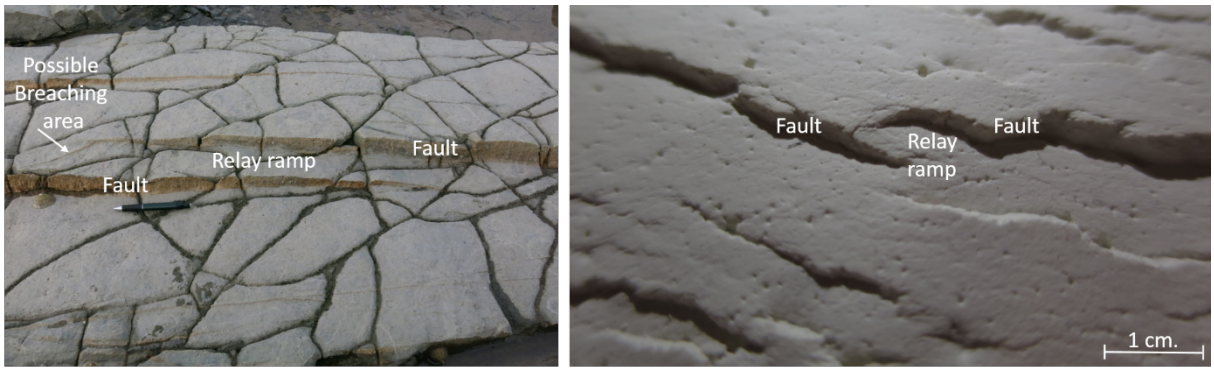

Fig. 6.2: (a) Field example of a relay ramp from Somerset, UK. A possible breaching area is pointed out. (Photo by David Peacock). (b) relay ramp from one of the analysed plaster models.

6.5.2 Fault linkage; Wasatch fault

Linking of fault segments is an important mechanism for fault growth, e.g. the Wasatch Fault, Utah and the Rangitaiki Fault, New Zealand. By studying analogue plaster models, we can gain more information about the evolution. The Wasatch Fault system in Utah is a 370 km long fault array which consists of ten fault segments that have become hard linked. The segment linkage of faults is reflected by a curved geometry in the linkage area (Machette et al., 1991). This curved geometry is well developed in the area around Salt Lake City and Provo (Fossen and Rotevatn, 2016). The fault system resembles modelled structures and shows a similar geometrical development as F3' found in model 5-15 (Fig. 6.3). The fault has several local minima and maxima along the strike due to the linking. This is consistent with nature. However, F3' becomes inactive as the deformation history of the model ceases due to the stiffness of the plaster. Nevertheless, it is likely that the fault will continue to develop in the same manner as the main faults in the different models. From the main faults in the different models, there is also evidence that parts of the faults become inactive while other parts of the faults still accumulate slip as the strain increases. This is in many ways consistent with nature where earthquakes accumulate slip in parts of the fault. The fault growth in analogue models is therefore valuable to understand the fault growth of all fault systems in nature, not just the Wasatch Fault system.

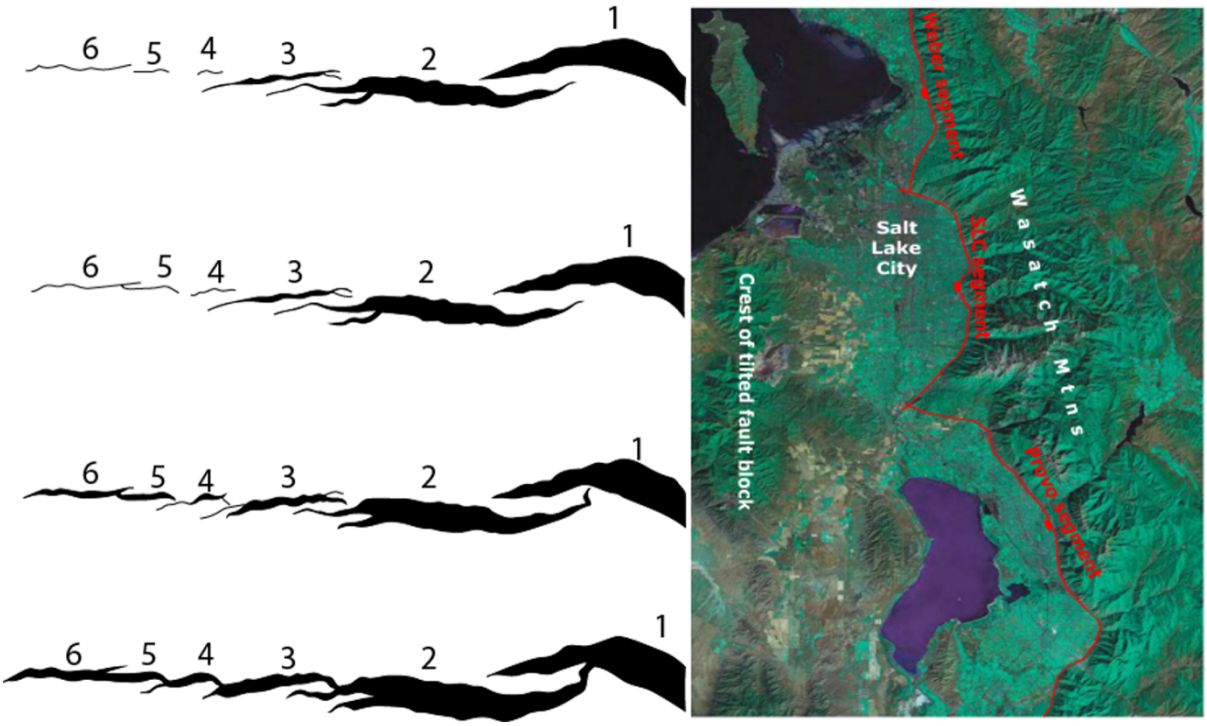

Fig. 6.3: To the left, fault growth from analogue plaster model (5-15) which illustrate the linkage between six fault segments. To the right, Wasatch fault with a typically curved symmetry in the linkage area between fault segments.

6.5.3 Maximum displacement-length relationship

A total of 44 faults were analysed to find the correlation between maximum displacement and fault length. The measurements can be fit to a relationship $D = cL^n$, which gives the material properties constant, $c = 0.0662$. By using this c value, the value of n is 0.95 in the analogue plaster models (Fig. 6.4a). Similar values for n have been recorded from natural fault systems and describe a nearly linear relationship. The displacement length data from the nature range over several orders of magnitude. To be able to compare the results from the analogue plaster models with nature, the maximum displacement-length is plotted in a logarithmic scale. The exponent n has been theoretical derived to be 1 (Cowie and Scholz, 1992a).

The scatter in field data has earlier been explained with measurement error (Mansfield and Cartwright, 2001, Cowie and Scholz, 1992a). However, measurement errors in analogue models are relatively small, and could not explain the deviation from the theoretical value of n. The viscosity of the plaster may however have an influence on the plaster behaviour as it increases with time and thus extension. A larger slip will develop in softer material, which means that the viscosity of the plaster when the fault was formed may affect the results. Nevertheless, Mansfield and Cartwright (2001) analysed this by comparing the faults from

different models. The result showed the effect of plaster viscosity is negligible. So what factors can explain the derivation from the theoretical value of *n*? The results from nature consider both immature and mature faults. Therefore, data from one area may have a low displacement/length-ratio whereas another fault may show a large displacement length ratio. This may explain why the value of *n* is not consistent in different data sets and is only close to 1 in the results from plaster models. Measurements from a single dataset may show derivation from the theoretical value (Fig. 6.4b) of *n,* but a logarithmic plot of several datasets are found to be linear or close to linear, $n = 1$ (Xu et al., 2006). This may indicate that the results from the analogue plaster model are trustworthy even though the dataset only ranges within one order of magnitude.

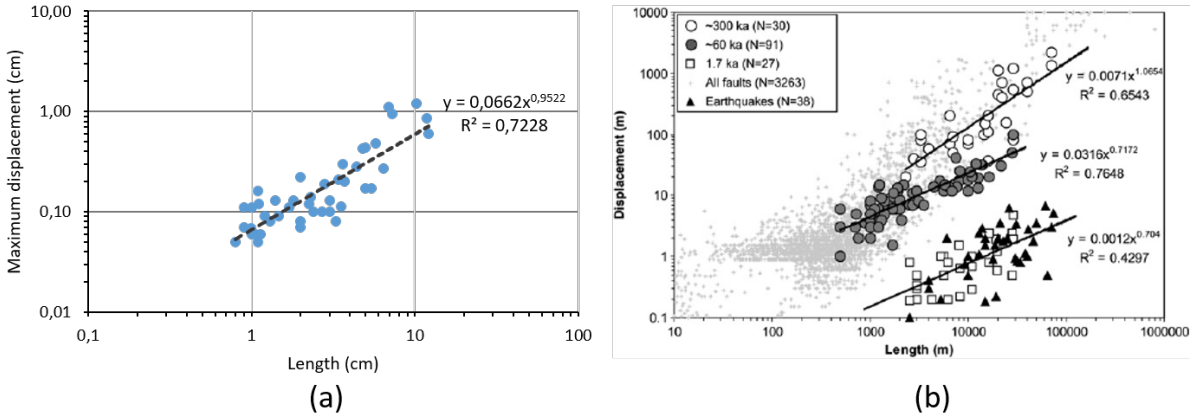

Fig. 6.4: Displacement length data plotted with log-log axis. (a) data-points from the analogue model with the best-fitted line (dashed line). The data from the analogue model can be correlated with the data from ~300 ka in (b) which is data from Nicol et al. (2010) showing the variations in displacement length for individual datasets.

6.6 Potential error sources

Although the results from the analogue models show similarities to natural structures associated with normal faults, some factors have to be taken into consideration when comparing models. Also, the interpretation of fault and fracture networks in ArcGIS has some pitfalls.

- Measurements of fault length and displacement have been done using a millimetre scale.
- The identification of nodes in the topological analysis is often clear, although in some cases it is more difficult and somewhat subjective, especially when it comes to minor fractures and 3D faults which have to be considered as 2D to fit the method that is used.

- The mixing characteristics of the plaster and water (rate, style and time) have an effect on the plaster's properties. The plaster becomes more viscous with mixing time. However, it is important to mix it long enough to prevent lumps of plaster in the mixture.
- Compared to nature, the plaster mix is homogenous, whereas the crust is heterogeneous. Also, syn- and post-deformational sedimentation occurs in nature, whereas in the plaster model, deformation (extension) of the model occurs without any sedimentation processes, which may affect the structures.
- Although the internal movable wall is moved by a handle with an almost constant rate, the movement of the internal wall often shifts from one side to the other due to the set-up. Due to this effect, the strain rate is not constant across the model, and changes during the experiment. According to Fossen and Gabrielsen (1996), an uneven strain rate may be consistent with fault growth associated with earthquakes.
- Air bubbles in the plaster-water mix are shown to have an influence on the propagation of faults and fractures at the surface. The faults and fractures typically curved toward these bubbles if they are large enough. However, in nature obstacles might also occur, having an influence on the behaviour to faults and fractures.

CHAPTER 7 – CONCLUSION

7.1 Conclusions

The main aims of this study have been to get a better understanding of fault growth, damage zone evolution and how the topology and thus connectivity of a fault system evolves with increasing strain. An analysis of six plaster models was done. These analogue models gave insights into faulting and fault-related damage. Structures found in analogue models show remarkably similar structures as in nature, and the following conclusions are drawn:

- The plaster models have shown to be highly depended on the plaster water-ratio and the settling time of the plaster before the experiment is performed.
- Fault growth in analogue plaster models is not consistent. Some faults grow via sympathetic increase of length and displacement where linkage of fault segments occurs in the buckling point in displacement-length plots. Other faults show a rapid increase of fault length with only minor tip propagation as the displacement is accommodated by increasing strain which is reflected by a nearly vertical growth curve. A third type of faults uses some time to develop their fault length (~one-third of the lifetime) whereas only minor amounts of slip are accumulated. Once the fault length has developed, accumulation of slip dominates (~two-thirds of the lifetime to the faults), and only minor tip propagation may occur. Some faults also show a resume of lengthening after accumulation of displacement has dominated.
- The maximum D/L relationship shows an almost linear trend. The n value in a dataset from analogue plaster models is 0.95 which is similar to the theoretical and most accepted value of $n = 1$. This similarity indicates that fault growth in analogue models can be used to get a better understanding of the growth in nature.
- Most hanging wall damage occurs late in the deformation process in all of the models when the main fault accumulates less displacement. Larger faults in the hanging wall start to develop when the main fault becomes inactive.
- The topological analysis of three different plaster models shows that the connectivity is generally greater in the footwall than in the hanging wall throughout the extension phase. The connectivity in the hanging wall is greater in a mature fault system than in an

immature fault system, whereas in the footwall, only small changes in the damage zone can be observed throughout the deformation process.

- The pathway of the evolution of the network occurs in a predictable way, as it increases with increasing strain. The proportion of Y-nodes, I-C branches and C-C branches increases with increasing strain. Therefore, the connectivity in a fault and fracture system increases with increasing strain.
- The modelling method used for this thesis has a relatively simple set-up and the results are remarkably similar to natural faults and related structures in addition to other analogue sand and plaster models. The similarities between nature and analogue models suggest that the development of both the analogue models and nature occur by following more or less the same processes. This means that by studying the analogue models, we can predict how the structures have formed and/or will continue to develop as the deformation in these areas continues. Hence, we can conclude that in a large picture, analogue models give insight into the deformation and evolution to the presented area.

7.2 Suggestions for further work

Further work with analogue modelling can be done, and the findings can potentially be valuable. For statistically more robust results, I would suggest a focus on the following points:

- Do a more detailed topological analysis of several models, and investigate the connectivity variations along strike of faults in analogue models. Compare this with natural field examples.
- Focus more on the basement influence on the fault geometry. This can be done by testing other basement materials.
- A more detailed analysis of the displacement/length evolution of faults in analogue plaster models.
- Investigate the different types of damage zones in plaster models. Tip-damage zone, relay ramp-damage zones and weal-damage zones.
- Analysis of the damage evolution in reverse and strike-slip faults.

REFERENCES

ACKERMANN, R. V., SCHLISCHE, R. W. & WITHJACK, M. O. 2001. The geometric and statistical evolution of normal fault systems: an experimental study of the effects of mechanical layer thickness on scaling laws. *Journal of Structural Geology,* 23**,** 1803-1819.

BERKOWITZ, B., BOUR, O., DAVY, P. & ODLING, N. 2000. Scaling of fracture connectivity in geological formations. *Geophys. Res. Lett,* 27**,** 2061-2064.

BRAATHEN, A., TVERANGER, J., FOSSEN, H., SKAR, T., CARDOZO, N., SEMSHAUG, S., BASTESEN, E. & SVERDRUP, E. 2009. Fault facies and its application to sandstone reservoirs. *Aapg Bulletin,* 93**,** 891-917.

BRUN, J.-P., SOKOUTIS, D. & VAN DEN DRIESSCHE, J. 1994. Analogue modeling of detachment fault systems and core complexes. *Geology,* 22**,** 319-322.

BUCHANAN, P. & MCCLAY, K. 1991. Sandbox experiments of inverted listric and planar fault systems. *Tectonophysics,* 188**,** 97-115.

BØYUM, M. 2015. Plaster modelling of fault development in extensional regimes (Master Thesis). Universitetet i Bergen, unpublished.

CADELL, H. M. 1888. *Experimental Researches in Mountain Building*.

CAINE, J. S., EVANS, J. P. & FORSTER, C. B. 1996. Fault zone architecture and permeability structure. *Geology,* 24**,** 1025-1028.

CARTWRIGHT, J. A., TRUDGILL, B. D. & MANSFIELD, C. S. 1995. Fault growth by segment linkage: an explanation for scatter in maximum displacement and trace length data from the Canyonlands Grabens of SE Utah. *Journal of Structural Geology,* 17**,** 1319-1326.

CLOOS, E. 1955. Experimental analysis of fracture patterns. *Geological Society of America Bulletin,* 66**,** 241-256.

COFFIN, G. K. & KUMAR, S. 1964. Plaster of Paris as a Static and Dynamic Model Testing Material. DTIC Document.

COWIE, P. A. & SCHOLZ, C. H. 1992a. Displacement-length scaling relationship for faults: data synthesis and discussion. *Journal of Structural Geology,* 14**,** 1149-1156.

COWIE, P. A. & SCHOLZ, C. H. 1992b. Growth of faults by accumulation of seismic slip. *Journal of Geophysical Research: Solid Earth,* 97**,** 11085-11095.

COWIE, P. A. & SCHOLZ, C. H. 1992c. Physical explanation for the displacement-length relationship of faults using a post-yield fracture mechanics model. *Journal of Structural Geology,* 14**,** 1133-1148.

CRIDER, J. G. & POLLARD, D. D. 1998. Fault linkage: three-dimensional mechanical interaction between echelon normal faults. *Journal of Geophysical Research: Solid Earth,* 103**,** 24373-24391.

DE JOUSSINEAU, G. & AYDIN, A. 2007. The evolution of the damage zone with fault growth in sandstone and its multiscale characteristics. *Journal of Geophysical Research: Solid Earth,* 112.

DUFFY, O. B., BELL, R. E., JACKSON, C. A. L., GAWTHORPE, R. L. & WHIPP, P. S. 2015. Fault growth and interactions in a multiphase rift fault network: Horda Platform, Norwegian North Sea. *Journal of Structural Geology,* 80**,** 99-119.

EISENSTADT, G. & SIMS, D. 2005. Evaluating sand and clay models: do rheological differences matter? *Journal of Structural Geology,* 27**,** 1399-1412.

ELLIS, P. G. & MCCLAY, K. R. 1988. Listric extensional fault systems - results of analogue model experiments. *Basin Research,* 1**,** 55-70.

FOSSEN, H. 2010. *Structural geology,* New York, Cambridge University Press.

FOSSEN, H. & GABRIELSEN, R. H. 1996. Experimental modeling of extensional fault systems by use of plaster. *Journal of Structural Geology,* 18**,** 673-687.

FOSSEN, H. & HESTHAMMER, J. 1997. Geometric analysis and scaling relations of deformation bands in porous sandstone. *Journal of Structural Geology,* 19**,** 1479-1493.

FOSSEN, H., JOHANSEN, T. E. S., HESTHAMMER, J. & ROTEVATN, A. 2005. Fault interaction in porous sandstone and implications for reservoir management; examples from southern Utah. *AAPG bulletin,* 89**,** 1593-1606.

FOSSEN, H. & ROTEVATN, A. 2016. Fault linkage and relay structures in extensional settings—A review. *Earth-Science Reviews,* 154**,** 14-28.

FOSSEN, H., SCHULTZ, R. A., SHIPTON, Z. K. & MAIR, K. 2007. Deformation bands in sandstone: a review. *Journal of the Geological Society,* 164**,** 755-769.

GILLESPIE, P. A., JJ T. WALSH & WATTERSON., J. 1992. Limitations of dimension and displacement data from single faults and the consequences for data analysis and interpretation. *Journal of Structural Geology,* 14**,** 1157-1172.

GRASEMANN, B., MARTEL, S. & PASSCHIER, C. 2005. Reverse and normal drag along a fault. *Journal of Structural Geology,* 27**,** 999-1010.

GRAVELEAU, F., MALAVIEILLE, J. & DOMINGUEZ, S. 2012. Experimental modelling of orogenic wedges: A review. *Tectonophysics,* 538**,** 1-66.

GUPTA, S., COWIE, P. A., DAWERS, N. H. & UNDERHILL, J. R. 1998. A mechanism to explain rift-basin subsidence and stratigraphic patterns through fault-array evolution. *Geology,* 26**,** 595-598.

HENZA, A. A., WITHJACK, M. O. & SCHLISCHE, R. W. 2010. Normal-fault development during two phases of non-coaxial extension: An experimental study. *Journal of Structural Geology,* 32**,** 1656-1667.

HENZA, A. A., WITHJACK, M. O. & SCHLISCHE, R. W. 2011. How do the properties of a pre-existing normal-fault population influence fault development during a subsequent phase of extension? *Journal of Structural Geology,* 33**,** 1312-1324.

HIGGS, W. & MCCLAY, K. 1993. Analogue sandbox modelling of Miocene extensional faulting in the Outer Moray Firth. *Geological Society, London, Special Publications,* 71**,** 141-162.

HUBBERT, M. K. 1937. Theory of scale models as applied to the study of geologic structures. *Geological Society of America Bulletin,* 48**,** 1459-1520.

HUS, R., ACOCELLA, V., FUNICIELLO, R. & DE BATIST, M. 2005. Sandbox models of relay ramp structure and evolution. *Journal of Structural Geology,* 27**,** 459-473.

IMBER, J., TUCKWELL, G. W., CHILDS, C., WALSH, J. J., MANZOCCHI, T., HEATH, A. E., BONSON, C. G. & STRAND, J. 2004. Three-dimensional distinct element modelling of relay growth and breaching along normal faults. *Journal of Structural Geology,* 26**,** 1897-1911.

JACKSON, C. A. L. & ROTEVATN, A. 2013. 3D seismic analysis of the structure and evolution of a salt-influenced normal fault zone: A test of competing fault growth models. *Journal of Structural Geology,* 54**,** 215-234.

JANSSEN, C., WAGNER, F., ZANG, A. & DRESEN, G. 2001. Fracture process zone in granite: a microstructural analysis. *International Journal of Earth Sciences,* 90**,** 46-59.

KEEP, M. & MCCLAY, K. 1997. Analogue modelling of multiphase rift systems. *Tectonophysics,* 273**,** 239-270.

KIM, Y.-S., PEACOCK, D. C. P. & SANDERSON, D. J. 2003. Mesoscale strike-slip faults and damage zones at Marsalforn, Gozo Island, Malta. *Journal of Structural Geology,* 25**,** 793-812.

KIM, Y.-S., PEACOCK, D. C. P. & SANDERSON, D. J. 2004. Fault damage zones. *Journal of Structural Geology,* 26**,** 503-517.

KIM, Y.-S. & SANDERSON, D. J. 2005. The relationship between displacement and length of faults: a review. *Earth-Science Reviews,* 68**,** 317-334.

KOYI, H. 1997. Analogue modelling: from a qualitative to a quantitative technique—a historical outline. *Journal of Petroleum Geology,* 20**,** 223-238.

KRISTENSEN, M. B., CHILDS, C., OLESEN, N. Ø. & KORSTGÅRD, J. A. 2013. The microstructure and internal architecture of shear bands in sand–clay sequences. *Journal of Structural Geology,* 46**,** 129-141.

LARSEN, P.-H. 1988. Relay structures in a Lower Permian basement-involved extension system, East Greenland. *Journal of Structural Geology,* 10**,** 3-8.

MACHETTE, M. N., PERSONIUS, S. F., NELSON, A. R., SCHWARTZ, D. P. & LUND, W. R. 1991. The Wasatch fault zone, utah—segmentation and history of Holocene earthquakes. *Journal of Structural Geology,* 13**,** 137-149.

MANIGHETTI, I., KING, G. C. P., GAUDEMER, Y., SCHOLZ, C. H. & DOUBRE, C. 2001. Slip accumulation and lateral propagation of active normal faults in Afar. *Journal of Geophysical Research: Solid Earth (1978–2012),* 106**,** 13667-13696.

MANSFIELD, C. & CARTWRIGHT, J. 2001. Fault growth by linkage: observations and implications from analogue models. *Journal of Structural Geology,* 23**,** 745-763.

MANZOCCHI, T. 2002. The connectivity of two-dimensional networks of spatially correlated fractures. *Water Resources Research,* 38.

MCCLAY, K. 1996. Recent advances in analogue modelling: uses in section interpretation and validation. *Geological Society, London, Special Publications,* 99**,** 201-225.

MCCLAY, K. & ELLIS, P. 1987. Geometries of extensional fault systems developed in model experiments. *Geology,* 15**,** 341-344.

MCCLAY, K. & SCOTT, A. 1991. Experimental models of hangingwall deformation in ramp-flat listric extensional fault systems. *Tectonophysics,* 188**,** 85-96.

MCCLAY, K. & WHITE, M. 1995. Analogue modelling of orthogonal and oblique rifting. *Marine and Petroleum Geology,* 12**,** 137-151.

MCCLAY, K. R. 1990. Extensional fault systems in sedimentary basins: a review of analogue model studies. *Marine and Petroleum Geology,* 7**,** 206-233.

MEAD, W. J. 1920. Notes on the mechanics of geologic structures. *Journal of Geology,* 28**,** 505-523.

MICARELLI, L., BENEDICTO, A. & WIBBERLEY, C. A. J. 2006a. Structural evolution and permeability of normal fault zones in highly porous carbonate rocks. *Journal of Structural Geology,* 28**,** 1214-1227.

MICARELLI, L., MORETTI, I., JAUBERT, M. & MOULOUEL, H. 2006b. Fracture analysis in the south-western Corinth rift (Greece) and implications on fault hydraulic behavior. *Tectonophysics,* 426**,** 31-59.

MITCHELL, T. & FAULKNER, D. 2009. The nature and origin of off-fault damage surrounding strike-slip fault zones with a wide range of displacements: a field study from the Atacama fault system, northern Chile. *Journal of Structural Geology,* 31**,** 802-816.

MORLEY, C. K. & NIXON, C. W. 2016. Topological characteristics of simple and complex normal fault networks. *Journal of Structural Geology,* 84**,** 68-84.

NICOL, A., WALSH, J., VILLAMOR, P., SEEBECK, H. & BERRYMAN, K. 2010. Normal fault interactions, paleoearthquakes and growth in an active rift. *Journal of Structural Geology,* 32**,** 1101-1113.

NIXON, C. W., BULL, J. M. & SANDERSON, D. J. 2014. Localized vs distributed deformation associated with the linkage history of an active normal fault, Whakatane Graben, New Zealand. *Journal of Structural Geology,* 69, Part A**,** 266-280.

PEACOCK, D. & SANDERSON, D. 1991. Displacements, segment linkage and relay ramps in normal fault zones. *Journal of Structural Geology,* 13**,** 721-733.

PEACOCK, D. & SANDERSON, D. 1994. Geometry and development of relay ramps in normal fault systems. *AAPG bulletin,* 78**,** 147-165.

RANALLI, G. 2001. Experimental tectonics: from Sir James Hall to the present. *Journal of Geodynamics,* 32**,** 65-76.

RECHES, Z. 1988. Evolution of fault patterns in clay experiments. *Tectonophysics,* 145**,** 141-156.

RYKKELID, E. & FOSSEN, H. 2002. Layer rotation around vertical fault overlap zones: observations from seismic data, field examples, and physical experiments. *Marine and Petroleum Geology,* 19**,** 181-192.

SAINT-GOBAIN. 2016. *Molda 3 normal* [Online]. http://www.saintgobainformula.com/Products/Plaster/Molda-3-Normal. [Accessed 15.04 2016].

SALES, J. K. 1987. TECTONIC MODELS, Tectonic models. *Structural Geology and Tectonics.* Springer.

SANDERSON, D. J. & NIXON, C. W. 2015. The use of topology in fracture network characterization. *Journal of Structural Geology,* 72**,** 55-66.

SCHLAGENHAUF, A., MANIGHETTI, I., MALAVIEILLE, J. & DOMINGUEZ, S. 2008. Incremental growth of normal faults: Insights from a laser-equipped analog experiment. *Earth and Planetary Science Letters,* 273**,** 299-311.

SCHLISCHE, R. W., YOUNG, S. S., ACKERMANN, R. V. & GUPTA, A. 1996. Geometry and scaling relations of a population of very small rift-related normal faults. *Geology,* 24**,** 683-686.

SCHULTZ-ELA, D. D., JACKSON, M. P. & VENDEVILLE, B. C. 1993. Mechanics of active salt diapirism. *Tectonophysics,* 228**,** 275-312.

SCHULTZ, R. A. & FOSSEN, H. 2002. Displacement–length scaling in three dimensions: the importance of aspect ratio and application to deformation bands. *Journal of Structural Geology,* 24**,** 1389-1411.

VAN DER PLUIJM, B. & MARSHAK, S. 2004. *Earth structure,* New York, W. W. Norton & Company, Inc

VENDEVILLE, B. C. & JACKSON, M. 1992. The rise of diapirs during thin-skinned extension. *Marine and Petroleum Geology,* 9**,** 331-354.

WALSH, J., BAILEY, W., CHILDS, C., NICOL, A. & BONSON, C. 2003. Formation of segmented normal faults: a 3-D perspective. *Journal of Structural Geology,* 25**,** 1251-1262.

WALSH, J., NICOL, A. & CHILDS, C. 2002. An alternative model for the growth of faults. *Journal of Structural Geology,* 24**,** 1669-1675.

WALSH, J. J. & WATTERSON, J. 1988. Analysis of the relationship between displacements and dimensions of faults. *Journal of Structural Geology,* 10**,** 239-247.

WU, J. E., MCCLAY, K., WHITEHOUSE, P. & DOOLEY, T. 2009. 4D analogue modelling of transtensional pull-apart basins. *Marine and Petroleum Geology,* 26**,** 1608-1623.

XU, S., NIETO-SAMANIEGO, A., ALANIZ-ÁLVAREZ, S. & VELASQUILLO-MARTINEZ, L. 2006. Effect of sampling and linkage on fault length and length–displacement relationship. *International Journal of Earth Sciences,* 95**,** 841-853.

APPENDIX A

This part contains additional information about analogue plaster models and attached videos and a summary of the work flow in ArcGIS 10.3.1 which have been used to analyse the photographs in proportion to the topological part of the thesis.

All videos show the experiment from top view.

Table with models and attached videos

Experiment	5-15	7-15	11-15	12-15	13-15	19-15
Video title (file size)	Video 5-15.mp4 (14,0 MB)	Video 7-15.mp4 (19,1 MB)	Video 11-15.mp4 (27,0 MB)	Video 12-15.mp4 (29,3 MB)	Video 13-15.mp4 (18,4 MB)	Video 19-15.mp4 (24,4 MB)
Time	24 sec.	33 sec.	37 sec.	42 sec.	29 sec.	37 sec.

APPENDIX B

Workflow in Arc GIS 10.3.1 and Excel

1. ArcCatalog and geodatabase file (gdb.) created to save and organize feature classes. These feature classes are used for interpreting and analysing the fault and fracture network in different pictures.
2. Picture added and scaled.
3. Feature class for the different features needed for the interpretation is created. I-nodes, Y-nodes and X-nodes is created as a point feature class. I-I branch, I-C branch and C-C branch is created as a polyline. Slip surface and sample area is created as a polygon. It is important to changes the measure box from “disable” to “enable” as this automatically calculate their length.

-

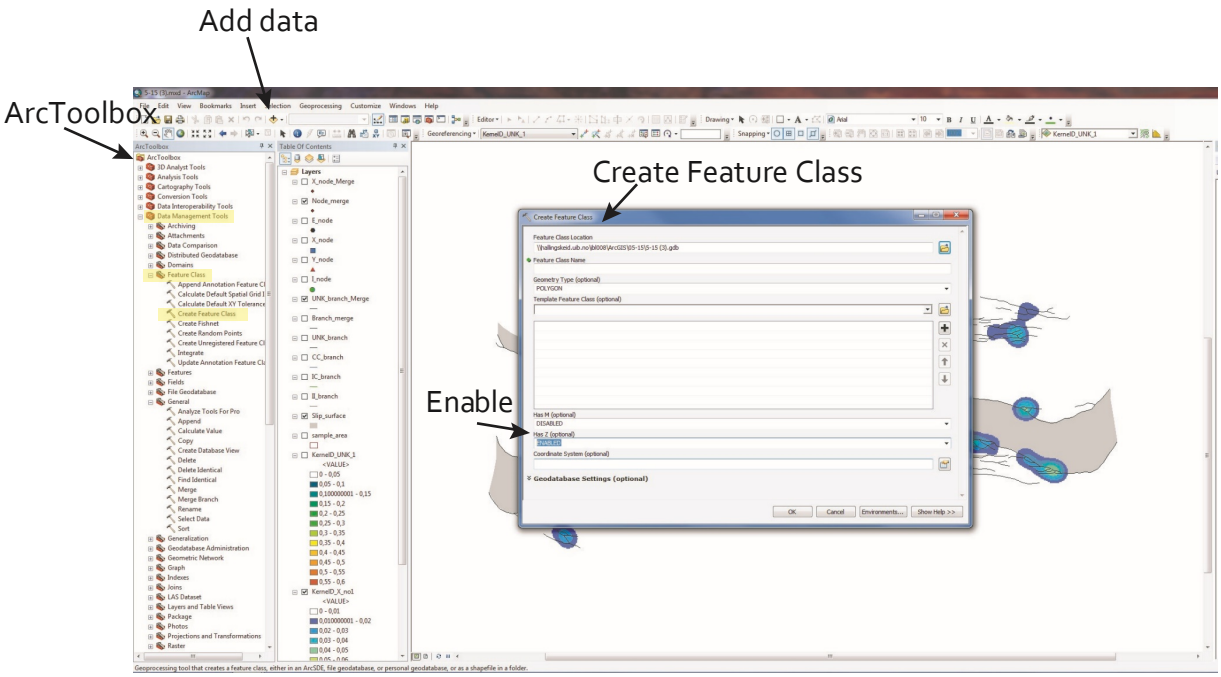

4. The features within the sample area is marked and the data extracted.
5. Merging of connecting nodes (Y and X nodes) and merging of all branches is done with the merge tool in Arc Toolbox.
6. The merged connected nodes and branches are then put into Kernel density to which creates contour plots of connecting node frequency and branch intensity.

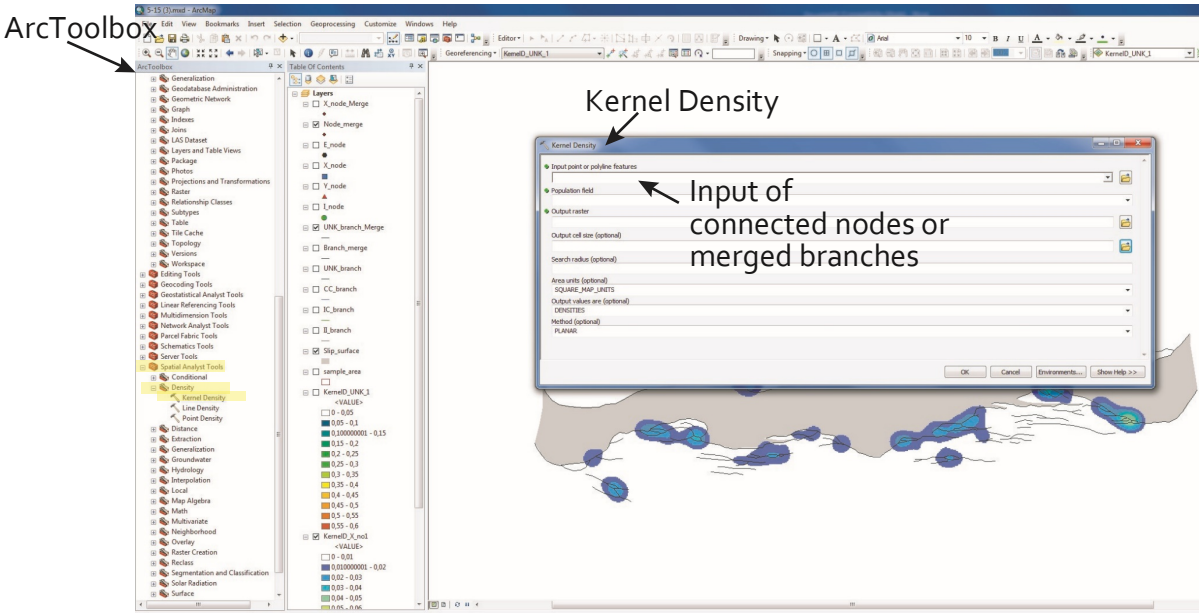

7. Changing of the scale of connecting node frequency and branch intensity to get the same scale at all of the contour plots with connecting node frequency and branch intensity. This is done in ‘Layer properties’

-

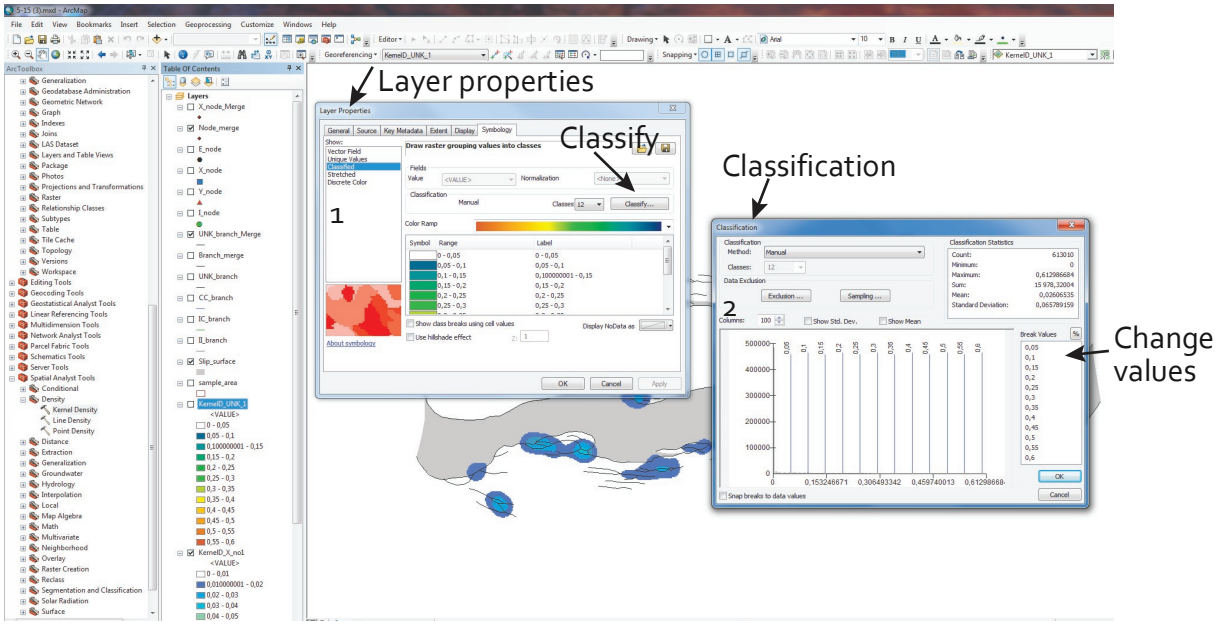

8. The extracted data is plotted in a Microsoft Excel sheet which calculates the proportion of the different nodes and branches, the connections per line and branch and their length, intensity and frequency.

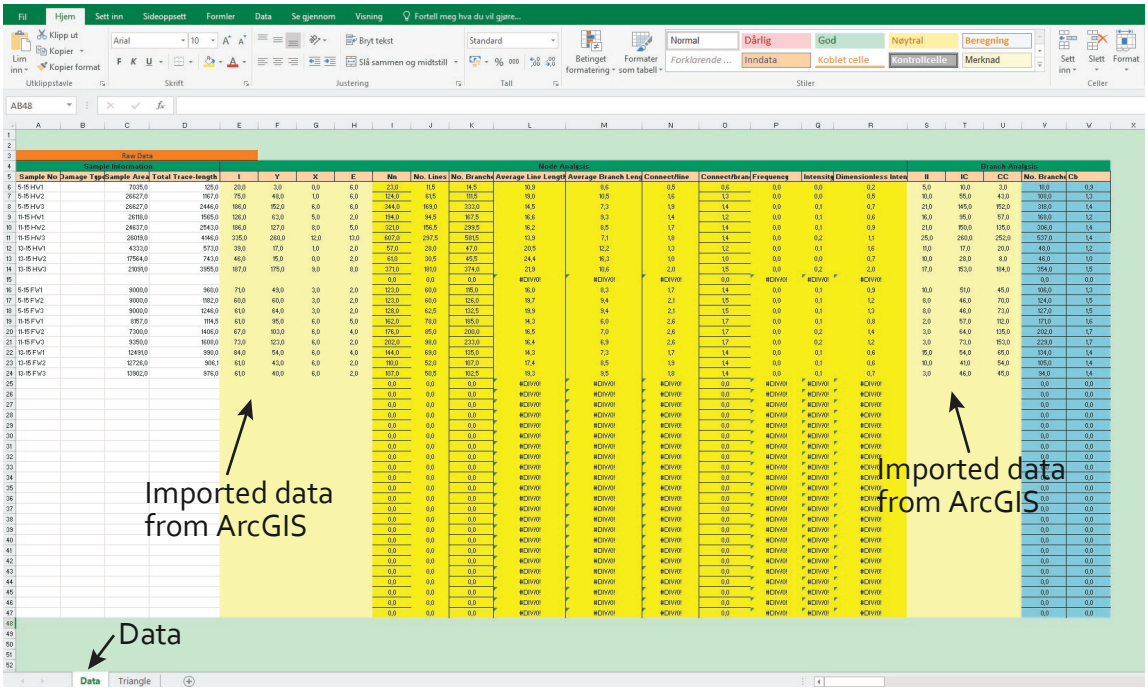
Imported data
from ArcGIS
Imported data
from ArcGIS
Data

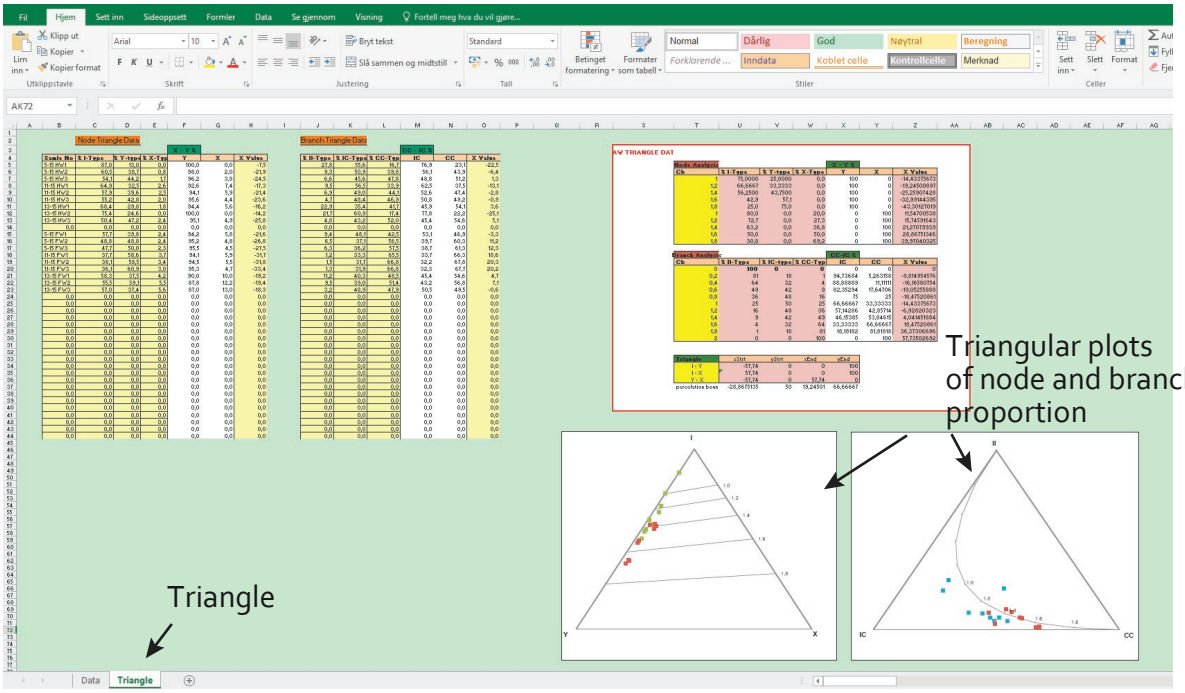
Triangular plots
of node and branch
proportion
Triangle